


Spring 5-2019

Design, Fabrication, and Characterization of Multilayer Hyperbolic Metamaterials

James Dilts

Follow this and additional works at: https://scholar.rose-hulman.edu/dept_optics

 Part of the [Optics Commons](#), and the [Other Engineering Commons](#)

Design, Fabrication, and Characterization of Multilayer Hyperbolic Metamaterials

A Thesis

Submitted to the Faculty

of

Rose-Hulman Institute of Technology

by

James Dilts

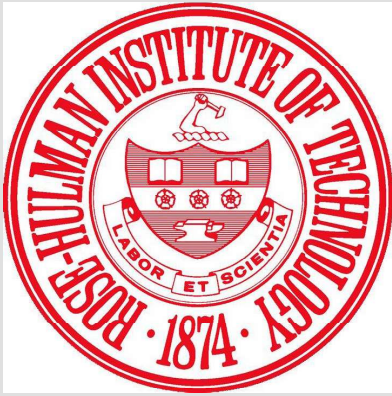
In Partial Fulfillment of the Requirements for the Degree

of

Master of Science in Optical Engineering

May 2019

©2019 James Dilts



ROSE-HULMAN INSTITUTE OF TECHNOLOGY

Final Examination Report

James Dilts

Optical Engineering

Name

Graduate Major

Thesis Title Design, Fabrication, and Characterization of Multilayer Hyperbolic Metamaterials

DATE OF EXAM:

April 18, 2019

EXAMINATION COMMITTEE:

Thesis Advisory Committee		Department
Thesis Advisor:	Hossein Alisafae	PHOE
	Azad Siahmakoun	PHOE
	Edward Wheeler	ECE

PASSED X

FAILED

ABSTRACT

James Dilts

M.S. O.E.

Rose-Hulman Institute of Technology

May 2019

Design, Fabrication, and Characterization of Multilayer Hyperbolic Metamaterials

Thesis Advisor: Dr. Hossein Alisafae

Hyperbolic metamaterials (HMMs) show extreme anisotropy, acting as metals and dielectrics along orthogonal directions. They are designed using the effective medium theory (EMT) and can be fabricated using standard semiconductor processing techniques. Current techniques used to characterize the optical behavior of HMMs have a high complexity or are unable to robustly determine the complex permittivity tensor. We describe the details of a procedure to obtain a very low mean-squared-error (MSE) for extraction of permittivity from hyperbolic metamaterials using spectroscopic ellipsometry. We have verified our procedure by fabricating three different samples of various materials and fill factors designed to have a response in the visible spectrum with an epsilon-near-zero (ENZ) region near the Helium-Neon (He-Ne) wavelength of 633 nm. The MSE obtained in each case has been less than 1.00. Our procedure eliminates the need for complicated ellipsometric measurements and modeling techniques, as well as the need for the addition of extra parts such as prisms. Therefore, the process can be easily adopted.

Keywords: Optical Engineering, Metamaterials, Hyperbolic Dispersion, Physical Vapor Deposition, Variable Angle Spectroscopic Ellipsometry

+*Ad Majorem Dei Gloriam*+

ACKNOWLEDGEMENTS

I would like to take this opportunity to thank my advisor Dr. Hossein Alisafae for his guidance and support over the past two years and for always being willing to chat about my research no matter what he was doing. He created an environment of academic support and openness that helped lead to the complete of this thesis. His example is one I hope to follow in my future work.

I would also like to thank my committee members Dr. Azad Siahmakoun from Physics and Optical Engineering and Dr. Edward Wheeler from Electrical and Computer Engineering for agreeing to be a part of my defense and for their contributions of knowledge and support to this project. Dr. Scott Kirkpatrick, Mr. Brian Fair, and the MiNDS facility were also instrumental in completing the fabrication of this project.

I am indebted to my classmates Jake and C.K. for working together on classwork and for their helpful critiques on my presentations and research. Additionally, C.K. assisted with the fabrication and measurement of several HMMs. I would also like to thank Ehsan for teaching me how to use the cleanroom facilities and ellipsometer, and for developing the \LaTeX format for this thesis.

Most importantly, I would like to thank my parents Connie and Steve and my brother Stuart for their unconditional support that led to this moment. I could not have done it without them.

TABLE OF CONTENTS

Contents

LIST OF FIGURES	iv
LIST OF TABLES	vi
LIST OF ABBREVIATIONS.....	vii
LIST OF SYMBOLS	ix
1. INTRODUCTION.....	1
2. THEORY AND BACKGROUND.....	5
2.1 Maxwell’s Equations.....	5
2.2 The Wave Equation	7
2.3 Negative Index Media	7
2.4 Propagation of Light in Various Materials.....	8
2.4.1 Isotropic Dielectrics	9
2.4.2 Conducting Media	13
2.4.3 Anisotropic Media.....	17
2.5 The Mueller Matrix.....	19
2.6 The Hyperbolic Dispersion Relation	21
2.7 Effective Medium Theory (EMT).....	23
3. DESIGN AND EFFECTIVE OPTICAL BEHAVIOR	26
3.1 HMM with ENZ near 633 nm.....	26
3.2 Al/TiO ₂ HMM	30
3.3 Biaxial HMM	32
3.4 Cu/Air HMM	36
4. FABRICATION AND CHARACTERIZATION.....	37
4.1 Fabrication	37
4.1.1 Thin Film Deposition Using EB-PVD	38
4.1.2 Device Fabrication.....	43
4.2 Characterization	46
4.2.1 Spectroscopic Ellipsometry	46
4.2.2 TIR Ellipsometry	48
4.2.3 Our Spectroscopic Ellipsometry Technique	49

5. DISCUSSION OF RESULTS.....	51
5.1 Summary	51
5.2 Material Constants	51
5.3 MSE Values.....	53
5.4 Surface Roughness.....	56
5.5 Cu/TiO ₂ HMM.....	57
5.5.1 EMA Model Spectroscopic Ellipsometry.....	57
5.5.2 TIR Ellipsometry	61
5.6 Cu/Air HMM	64
5.7 Al/TiO ₂ HMM	65
6. CONCLUSION.....	67
6.1 Future Work	68
LIST OF REFERENCES	69
APPENDICES	75
APPENDIX A - MATLAB CODES.....	76
A.1 Surface Plots of Permittivity vs. Wavelength and Fill Factor.....	76
A.2 Surface Plots for Biaxial Metamaterials	79
A.3 Effective Medium Theory Calculations	82
A.4 Effective Medium Theory Calculations for Biaxial Metamaterials.....	87
A.5 Compare Effective Medium Theory Calculations to Measured Values.....	91
A.6 Plotting the Hyperbolic Isofrequency Curve	99

LIST OF FIGURES

Figure	Page
Figure 1.1: Schematic of an HMM device and its dispersion relations.....	2
Figure 2.1: Optical constants vs. frequency for a dielectric	12
Figure 2.2: Index of refraction plotted versus frequency for a metal.	16
Figure 2.3: Effective media theory	24
Figure 2.4: Screening factor for different arrangements of composites	25
Figure 3.1: Permittivity response with respect to wavelength and fill factor	27
Figure 3.2: The expected electrical permittivity of the Cu/TiO ₂ HMM.....	28
Figure 3.3: The Cu/TiO ₂ isofrequency curve at 633 nm	28
Figure 3.4: Cross-section of the final 15 nm Cu/TiO ₂ design	29
Figure 3.5: The expected permittivity for a Al/TiO ₂ HMM.....	30
Figure 3.6: Al/TiO ₂ Surface Plot.....	31
Figure 3.7: Al/TiO ₂ Surface Plot.....	31
Figure 3.8: The indices of refraction for OAD deposited TiO ₂	32
Figure 3.9: The surface plot for a biaxial Cu/TiO ₂ metamaterial.....	33
Figure 3.10: The expected electric permittivity of the biaxial HMM.....	35
Figure 3.11: Zoomed-in view of the biaxial HMM response	35
Figure 3.12: The expected permittivity of the OAD deposited Cu.....	36
Figure 4.1: Crucible filled with Cu.....	40
Figure 4.2: Crucible with TiO ₂	41
Figure 4.3: PVD 75 used for HMM fabrication	41
Figure 4.4: Fabrication Chamber.....	44
Figure 4.5: Spectroscopic ellipsometry configuration used in this work.	46
Figure 4.6: The α -SE Ellipsometer	48

Figure 4.7: The spectroscopic ellipsometric process developed in this work for extracting the permittivity of HMMs.....	50
Figure 5.1: The index of refraction of the deposited TiO ₂ determined by spectroscopic ellipsometry.....	52
Figure 5.2: The optical constants of the deposited Cu determined by spectroscopic ellipsometry.....	52
Figure 5.3: The Ψ and Δ model compared to the measured values.....	55
Figure 5.4: AFM measurements of surface roughness.....	56
Figure 5.5: The expected index of refraction based on EMT with in-house measured permittivity values compared to the fabricated device as measured by spectroscopic ellipsometry.	57
Figure 5.6: The permittivities based on EMT with in-house measured permittivity values compared to the fabricated device as measured by spectroscopic ellipsometry.	58
Figure 5.7: Results from the Cu/TiO ₂ multilayers.....	60
Figure 5.8: TIR Ellipsometry Measured Indices of Refraction.....	62
Figure 5.9: TIR Ellipsometry Measured Permittivities.....	63
Figure 5.10: Ellipsometry Measured Permittivities of Cu/TiO ₂	64
Figure 5.11: Ellipsometry Measured Permittivities of Al/TiO ₂	66

LIST OF TABLES

Table	Page
Table 5.1: MSE Values for SE procedure described here.	54
Table 5.2: MSE Values reported elsewhere.....	54
Table 5.3: Surface roughness as measured by AFM	56

LIST OF ABBREVIATIONS

AC	Alternating Current
AFM	Atomic Force Microscope
ALD	Atomic Layer Deposition
CVD	Chemical Vapor Deposition
CMOS	Complementary Metal-Oxide Semiconductor
DC	Direct Current
EMA	Effective Medium Approximation
EMT	Effective Medium Theory
ENZ	Epsilon-near-zero
HF	Hydrofluoric Acid
HMM	Hyperbolic Metamaterial
IE	Interference Ellipsometry
MiNDS	Micro-Nanoscale Device Systems Laboratory
MM	Mueller Matrix
MSE	Mean Squared Error
OAD	Oblique Angle Deposition
PLD	Pulsed Laser Deposition
PVD	Electron-Beam Physical Vapor Deposition
SE	Spectroscopic Ellipsometry
SE+T	Spectroscopic and Transmission Ellipsometry
SEM	Scanning Electron Microscopy

SPP	Surface Plasmon Polariton
TE	Transverse Electric
TIR	Total Internal Reflection
TM	Transverse Magnetic
TMM	Transfer-Matrix Method
UV	Ultraviolet

LIST OF SYMBOLS

English Symbols

a_i	Ellipsoid Semiaxis
a_j	Ellipsoid Semiaxis
a_k	Ellipsoid Semiaxis
c	Speed of Light in Vacuum
\vec{B}	Magnetic Induction Vector
C	Bounded Ellipsometric Parameter
\vec{D}	Electric Displacement Vector
D	Ellipsometric Parameter
\vec{D}_0	Electric Displacement of Zeroth Medium
\vec{D}_1	Electric Displacement of First Medium
\vec{D}_2	Electric Displacement of Second Medium
\vec{D}_{av}	Average Electric Displacement
D_x	Electric Displacement Along the x -axis
D_y	Electric Displacement Along the y -axis
D_z	Electric Displacement Along the z -axis
\vec{E}	Electric Field Vector
\vec{E}_1	Electric Field of First Medium
\vec{E}_2	Electric Field of Second Medium
\vec{E}_{av}	Average Electric Field

e	Charge of an Electron
\vec{H}	Magnetic Field Vector
i	Imaginary Unit
\vec{J}	Electric Current Density
k	Absorption Coefficient
\mathcal{K}	Complex Wavenumber
K	Elastically Bound Force Constant
\vec{k}	Wave Vector
k_0	Vacuum Wave Number
k_x	x -Component of Wavenumber
k_y	y -Component of Wavenumber
k_z	z -Component of Wavenumber
\vec{M}	Magnetization
m	Mass of an Electron
$m_{i,j}$	Matrix Element
N	Bounded Ellipsometric Parameter
\mathcal{N}	Complex Index of Refraction
N	Number of Electrons per Volume
n	Refractive Index
n_0	Vacuum Refractive Index
n_x	Principal Refractive Index Along the x -axis
n_y	Principal Refractive Index Along the y -axis
n_z	Principal Refractive Index Along the z -axis

\vec{P}	Material Polarization
p	Parallel Polarization
q	Lorentz Depolarization
\vec{r}	Displacement Position
r_p	Complex Amplitude Reflectance for p Polarization
r_s	Complex Amplitude Reflectance for s Polarization
S	Bounded Ellipsometric Parameter
s	Perpendicular Polarization
s	Surface of Integration
t	Time
t_p	Complex Amplitude Transmittance for p Polarization
t_s	Complex Amplitude Transmittance for s Polarization
u	Phase Velocity of a Wave
\vec{v}	Velocity of an Electron
z	Optical Axis

Greek Symbols

2α	Absorption Coefficient
α	Deposition Angle
α	Off-Diagonal, Second-Order Jones Matrix Element
β	Off-Diagonal, Second-Order Jones Matrix Element
γ	Mechanical Damping Proportionality Constant

Δ	Ellipsometric Phase Difference
δ	Skin Depth
ε	Electric Permittivity
ε_0	Electric Permittivity in Vacuum
ε_1	Electric Permittivity of First Medium
ε_2	Electric Permittivity of Second Medium
ε_D	Electric Permittivity of a Dielectric
ε_{eff}	Effective Electric Permittivity
ε_{ij}	Dielectric Permittivity Tensor
ε_M	Electric Permittivity of a Metal
ε_r	Relative Electric Permittivity
ε_x	x -Component of Electric Permittivity
ε_y	y -Component of Electric Permittivity
ε_z	z -Component of Electric Permittivity
ζ	Ellipsometric Parameter
η_{ij}	Impermeability Tensor
θ	Measurement Angle
κ	Screening Factor
λ	Wavelength
λ_0	Vacuum Wavelength
μ	Magnetic Permeability
μ_0	Magnetic Permeability in Vacuum
μ_r	Relative Magnetic Permeability

ξ	Ellipsometric Parameter
ρ	Electric Charge Density
σ	Electric Conductivity
τ	Time Constant
Ψ	Ellipsometric Amplitude Component
χ	Electric Susceptibility
ω	Angular Frequency
ω_0	Effective Resonance Frequency
ω_p	Plasma Frequency

1. INTRODUCTION

Metamaterials are subwavelength engineered media that produce optical responses beyond conventional media, such as a negative index of refraction [1], subwavelength imaging [2], and perfect absorption [3]. These responses occur due to effects such as the excitation of surface plasmon polaritons (SPPs) [4]. They have a wide range of applications such as photovoltaics [5], optical cloaking, achromatic flat lenses [6], superresolution [7], Purcell enhancement of spontaneous radiation [8, 9], and the development of planar optics [10] due to their ability to manipulate the near field of light [11].

Hyperbolic metamaterials (HMMs) exhibit a further interesting property with the hyperbolic shape of their isofrequency surfaces (Figure 1.1) — extreme anisotropy where they act like a metal and a dielectric in orthogonal directions [12]. HMMs can be realized as either an array of nanowires [13] or as alternating layers of dielectrics and metals [14] (Fig. 1.1) as long as the observer is not in the near field [15]. The coupling of the SPPs on each of the metal-dielectric boundaries leads to an effective response [16] as modeled in Section 2.7.

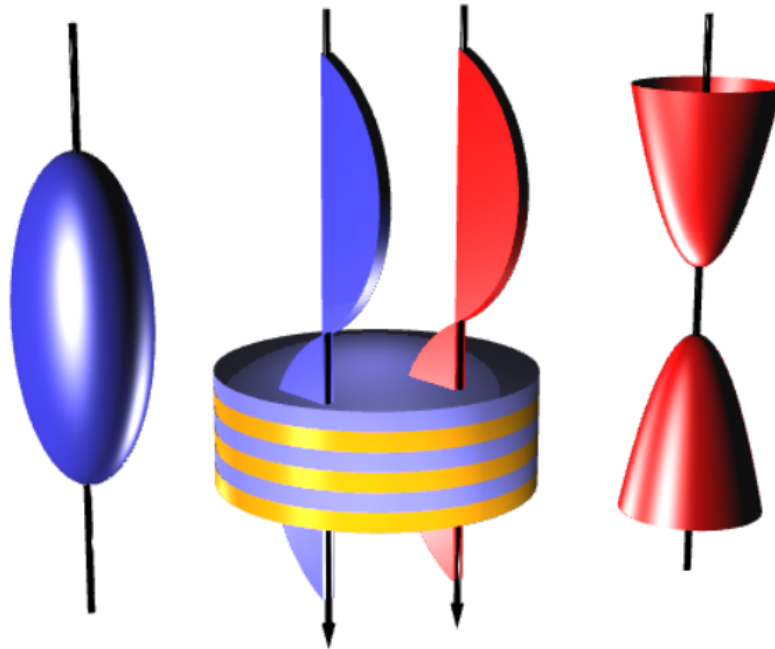


Figure 1.1: A schematic of an HMM device and its dispersion relations. The HMM is based on subwavelength gratings (middle). At shorter wavelengths, it has the same dispersion relation as conventional media (left), and at longer wavelengths the device will have a hyperbolic dispersion relation (right).

When it comes to practical aspects, it has unfortunately been a challenge to characterize the properties of HMMs with minimal error. This is especially important when the application is a sensor where any material error could translate into larger errors in the output, producing possible false positives. The Effective Medium Theory (EMT) values provide a reasonable approximation of the HMM behavior but do not take into account factors such as variations in deposited permittivities, layer thickness, surface roughness, and mechanical strain. These variations have led to the use of spectroscopic ellipsometry to measure the permittivities of as-fabricated HMMs, for which there have been numerous attempts for accurate characterization [17–19]. However, non-negligible discrepancies have been reported [20] with spectroscopic ellipsometry. Alternative ellipsometric techniques include interference enhancement (IE) ellipsometry, where the substrate is coated to increase light-HMM interactions [21]. In addition, transmission mode measurement to the reflection mode ellipsometry (SE+T) has been employed [22], but it still does not have the ability to characterize the out-of-plane behavior of extremely anisotropic HMMs accurately.

Another technique known as total internal reflection (TIR) ellipsometry uses a prism to couple light into the sample after it undergoes total internal reflection [23], which improves the characterization of thin semitransparent films [24] and has previously been used to successfully characterize HMMs [20].

We describe the details of a technique which is able to extract the out-of-plane permittivity through the use of EMT approximations which are much simpler to implement than the TIR models. It does not require any additional equipment or sample preparation and is able to be used with in-line processing. It can therefore be easily adopted to characterize metamaterial behavior.

For comparison purposes, we treat HMMs as uniaxial, homogeneous materials in the ellipsometric modeling [25]. We expect the in-plane results of spectroscopic ellipsometry to match well

with the EMT calculations. In addition, we attempt to eliminate the non-negligible discrepancy between the EMT values and the out-of-plane z direction caused by the anisotropic behavior of the HMM. This discrepancy is attributed to the incident light being inhibited from crossing the surface beyond evanescent penetration for any angle [20]. Overall, our goal is to obtain low-Mean Squared Error (MSE) values for characterizations of HMMs using spectroscopic ellipsometry. The intention of the thesis is to model, simulate, fabricate, and successfully characterize a hyperbolic metamaterial. Its organization is as follows:

[Chapter 2](#) discusses the background theory necessary to design, fabricate, and characterize HMMs including the effective medium theory as well as the dispersion relation derived from first principals. Additional information is provided about the propagation of light in several kinds of media.

[Chapter 3](#) presents the expected behavior of the HMM based on the effective medium theory. The design process used to achieve the desired permittivity behavior is explained.

[Chapter 4](#) discusses the fabrication procedure for HMMs using standard semiconductor fabrication processes. Additionally, the methods of spectroscopic ellipsometry used to characterize the fabricated samples are explained, including the material models used.

[Chapter 5](#) discusses results from the measurements in [Chapter 4](#). The ellipsometric results are presented and compared to expected values. It is shown that the results from the EMT ellipsometric modeling procedure are in good agreement with the theoretical model and have a low MSE.

[Chapter 6](#) concludes the thesis and provides suggestions for future work.

2. THEORY AND BACKGROUND

2.1. Maxwell's Equations

There are several ways to model the propagation of light. In this thesis, the vector electromagnetic model will be used based on Maxwell's Equations. The electromagnetic state of matter can be described using the four quantities

1. The volume density of electric charge ρ
2. The volume density of electric dipoles, also called polarization \vec{P}
3. The volume density of magnetic dipoles or magnetization \vec{M}
4. The electric current per unit density, know as the current density \vec{J}

These values are related to the electric field \vec{E} and magnetic field \vec{H} by Maxwell's equations [26]

$$\vec{\nabla} \times \vec{E} = -\mu_0 \frac{\partial \vec{H}}{\partial t} - \mu_0 \frac{\partial \vec{M}}{\partial t}, \quad (2.1)$$

$$\vec{\nabla} \times \vec{H} = \epsilon_0 \frac{\partial \vec{E}}{\partial t} + \frac{\partial \vec{P}}{\partial t} + \vec{J}, \quad (2.2)$$

$$\vec{\nabla} \cdot \vec{E} = -\frac{1}{\epsilon_0} \vec{\nabla} \cdot \vec{P} + \frac{\rho}{\epsilon_0}, \quad (2.3)$$

$$\vec{\nabla} \cdot \vec{H} = -\vec{\nabla} \cdot \vec{M}, \quad (2.4)$$

By substituting the electric displacement $\vec{D} = \epsilon_0 \vec{E} + \vec{P}$ and the magnetic induction $\vec{B} = \mu_0(\vec{H} + \vec{M})$,

Maxwell's equations assume the familiar form

$$\vec{\nabla} \times \vec{E} + \frac{\partial \vec{B}}{\partial t} = 0, \quad (2.5)$$

$$\vec{\nabla} \times \vec{H} - \frac{\partial \vec{D}}{\partial t} = \vec{J}, \quad (2.6)$$

$$\vec{\nabla} \cdot \vec{D} = \rho, \quad (2.7)$$

$$\vec{\nabla} \cdot \vec{B} = 0, \quad (2.8)$$

Each of these equations represents empirical observations—Equation 2.5 Faraday’s law of electromagnetic induction, Equation 2.6 the modified Ampere’s law, Equation 2.7 Gauss’s law, and Equation 2.8 the absence of magnetic monopoles [27]. They predict the speed of light to be

$$\frac{\vec{E}}{\vec{B}} = \frac{1}{\sqrt{\epsilon_0 \mu_0}} = c, \quad (2.9)$$

where $c = 2.9979246 \times 10^8$ m/s is the speed of light in a vacuum [28].

The response of the conduction electrons to the electric field is given by Ohm’s Law

$$\vec{J} = \sigma \vec{E}, \quad (2.10)$$

where σ is the electric conductivity. The constitutive relations

$$\vec{D} = \epsilon \vec{E}, \quad (2.11)$$

and

$$\vec{B} = \mu \vec{H}, \quad (2.12)$$

can be used to describe the responses of the bound charges to the electric and magnetic fields, respectively. An alternative way to describe this response is

$$\vec{P} = (\epsilon - \epsilon_0) \vec{E} = \vec{\chi} \epsilon_0 \vec{E}, \quad (2.13)$$

where the proportionality factor

$$\vec{\chi} = \frac{\epsilon}{\epsilon_0} - 1, \quad (2.14)$$

is known as the electric susceptibility [29].

2.2. The Wave Equation

In nonmagnetic, electrically neutral media, Maxwell's Equations reduce to

$$\vec{\nabla} \times \vec{E} = -\mu_0 \frac{\partial \vec{B}}{\partial t}, \quad (2.15)$$

$$\vec{\nabla} \times \vec{H} = \epsilon_0 \frac{\partial \vec{E}}{\partial t} + \frac{\partial \vec{P}}{\partial t} + \vec{J}, \quad (2.16)$$

$$\vec{\nabla} \cdot \vec{E} = -\frac{1}{\epsilon_0} \vec{\nabla} \cdot \vec{P}, \quad (2.17)$$

$$\vec{\nabla} \cdot \vec{H} = 0. \quad (2.18)$$

By taking the curl of Equation 2.15, the time derivative of Equation 2.16, and eliminating \vec{H} , the general wave equation becomes

$$\vec{\nabla} \times (\vec{\nabla} \times \vec{E}) + \frac{1}{c^2} \frac{\partial^2 \vec{E}}{\partial t^2} = -\mu_0 \frac{\partial^2 \vec{P}}{\partial t^2} - \mu_0 \frac{\partial \vec{J}}{\partial t}, \quad (2.19)$$

with the two terms on the right-hand side of the equation known as source terms. The source terms model the material polarization and conduction current density, respectively. In nonconducting media, the current density is neglected and the polarization source term $-\mu_0 \partial^2 \vec{P} / \partial t^2$ explains the optical behavior of the material. This term can be used to explain several optical properties of a dielectric including dispersion, absorption, and double refraction in addition to others. The conduction term $-\mu_0 \partial \vec{J} / \partial t$ becomes dominant in conducting media and can be used to explain the high reflectivity (or "shininess") and large opacity of good conductors. Although it will not be covered here, both terms must be taken into account in semiconductors [29].

2.3. Negative Index Media

First theorized by V. G. Veselago [30], media with a negative index of refraction can be fabricated through the use of periodic resonant structures. A negative refractive index will be obtained when

both the electric permittivity and magnetic permeability have negative values. A flat slab of a doubly-negative material will focus light to a point, acting as a lens [30]. Such materials were initially met with skepticism until the first empirical demonstration of a negative index material [1]. Interest has continued to grow as fabrication techniques improve.

The index of refraction can be found using the following relation:

$$n = \sqrt{\epsilon_r \mu_r}. \quad (2.20)$$

Assuming that both the permittivity and permeability have a value of negative one, the equation then becomes

$$n = \sqrt{(-1)(-1)}. \quad (2.21)$$

Using Euler's identity $e^{i\pi} + 1 = 0$, the refractive index can be expressed as

$$n = \sqrt{e^{2i\pi}}, \quad (2.22)$$

which is equivalent to

$$n = e^{i\pi} = -1. \quad (2.23)$$

Additionally, materials with a hyperbolic dispersion relation can have negative refraction; however, this is a result of dispersion and not of a doubly negative material [13].

2.4. Propagation of Light in Various Materials

This section describes the propagation of light in various types of media based on Maxwell's equations.

2.4.1. Isotropic Dielectrics

A nonconducting, isotropic medium consists of a material where the electrons are permanently bound to their atoms with no preferential direction. The material polarization \vec{P} can be found by assuming that each electron with a charge $-e$ is displaced by a position \vec{r} from its equilibrium, and is given by

$$\vec{P} = -Ne\vec{r}, \quad (2.24)$$

where N is the amount of electrons per volume. Assuming an elastically bound force constant K as a result of an applied electric field \vec{E} , the force equation is

$$-e\vec{E} = K\vec{r}. \quad (2.25)$$

Therefore, the static material polarization is expressed as

$$\vec{P} = \frac{Ne^2}{K}\vec{E} \quad (2.26)$$

It should be noted that this equation does not applied to a time varying electric field.

To represent the motion of the electrons, a classical damped harmonic oscillator is used, with an equation of motion

$$m\frac{d^2\vec{r}}{dt^2} + m\gamma\frac{d\vec{r}}{dt} + K\vec{r} = -e\vec{E}, \quad (2.27)$$

where $m\gamma(d\vec{r}/dt)$ represents a damping force with a proportionality constant $m\gamma$. The magnetic force is neglected in this equation because it is much smaller than the electric force in electromagnetic fields [29]. If the applied electric field and resulting motion of the electrons vary harmonically with time as $e^{-i\omega t}$, Equation 2.27 becomes

$$(-m\omega^2 - i\omega m\gamma + K)\vec{r} = -e\vec{E}, \quad (2.28)$$

with the polarization

$$\vec{P} = \frac{Ne^2}{-m\omega^2 - i\omega m\gamma + K} \vec{E}. \quad (2.29)$$

Equation 2.29 can be rewritten as

$$\vec{P} = \frac{Ne^2/m}{\omega_0^2 - \omega - i\omega\gamma} \vec{E}, \quad (2.30)$$

in which ω_0 is defined as

$$\omega_0 = \sqrt{\frac{K}{m}}, \quad (2.31)$$

and is known as the effective resonance frequency of the bound electrons. Equation 2.30 shows that there will be an optical resonance near the frequency ω_0 .

Next, the effect of polarization on the the propagation of light will be examined. The general wave equation (Equation 2.19) is used, with a conduction term of zero. Substituting Equation 2.30 into the polarization term gives the wave equation as

$$\vec{\nabla} \times (\vec{\nabla} \times \vec{E}) + \frac{1}{c^2} \frac{\partial^2 \vec{E}}{\partial t^2} = \frac{-\mu_0 Ne^2}{m} \left(\frac{1}{\omega_0^2 - \omega - i\omega\gamma} \right) \frac{\partial^2 \vec{E}}{\partial t^2}. \quad (2.32)$$

Since there is a linear relationship between \vec{P} and \vec{E} , it follows that $\vec{\nabla} \cdot \vec{E} = 0$ and therefore

$\vec{\nabla} \times (\vec{\nabla} \times \vec{E}) = -\vec{\nabla}^2 \vec{E}$. This reduces the above wave equation to

$$\vec{\nabla}^2 \vec{E} = \frac{1}{c^2} \left(1 + \frac{Ne^2}{m\epsilon_0} \cdot \frac{1}{\omega_0^2 - \omega - i\omega\gamma} \right) \frac{\partial^2 \vec{E}}{\partial t^2}, \quad (2.33)$$

after using the relation $1/c^2 = \mu_0\epsilon_0$ and rearranging terms.

To solve the differential equation, it is assumed that the final solution will be a homogeneous plane harmonic wave of the form

$$\vec{E} = \vec{E}_0 e^{i(\mathcal{K}z - \omega t)}, \quad (2.34)$$

where \mathcal{K} is the complex wavenumber expressed as

$$\mathcal{K} = k + i\alpha. \quad (2.35)$$

The index of refraction will also be complex as

$$\mathcal{N} = n + ik. \quad (2.36)$$

The complex index of refraction and wavenumber are related to each other as

$$\mathcal{K} = \frac{\omega}{c} \mathcal{N}. \quad (2.37)$$

By substituting Equation 2.34 into Equation 2.33, it can be found that a solution exists provided that

$$\mathcal{K}^2 = \frac{\omega^2}{c^2} \left(1 + \frac{Ne^2}{m\epsilon_0} \cdot \frac{1}{\omega_0^2 - \omega - i\omega\gamma} \right). \quad (2.38)$$

Equation 2.34 can then be written as

$$\vec{E} = \vec{E}_0 e^{-\alpha z} e^{i(kz - \omega t)}. \quad (2.39)$$

The absorption term $e^{-\alpha z}$ shows that the wave amplitude decays exponentially with distance as the energy of the wave is absorbed by the propagating medium. Since the energy of the wave will be proportional to $|\vec{E}|^2$, the energy will vary with distance as $e^{-2\alpha z}$. Therefore, the property 2α is known as the absorption coefficient, and the imaginary part of the complex index of refraction k is known as the absorption index. The two variables α and k are related by

$$\alpha = \frac{\omega}{c} k. \quad (2.40)$$

The phase factor in Equation 2.39 $e^{i(kz - \omega t)}$ shows that there is a harmonic wave with phase velocity u

$$u = \frac{\omega}{k} = \frac{c}{n}. \quad (2.41)$$

Combining Equations 2.37 and 2.38 indicates

$$\mathcal{N}^2 = (n + ik)^2 = 1 + \frac{Ne^2}{m\epsilon_0} \left(\frac{1}{\omega_0^2 - \omega - i\omega\gamma} \right). \quad (2.42)$$

Equating the real and imaginary parts gives the equations

$$n^2 - k^2 = 1 + \frac{Ne^2}{m\epsilon_0} \left(\frac{\omega_0^2 - \omega^2}{(\omega_0^2 - \omega^2)^2 + \omega^2\gamma^2} \right), \quad (2.43a)$$

$$2nk = \frac{Ne^2}{m\epsilon_0} \left(\frac{\gamma\omega}{(\omega_0^2 - \omega^2)^2 + \omega^2\gamma^2} \right), \quad (2.43b)$$

from which the optical constants n and k can be found.

A graph of these optical constants are shown in Figure 2.1 which assumes a general case of the frequency dependence of n and k . The absorption is strongest around the resonance frequency ω_0 and is close to zero at all other frequencies. The index of refraction is close to 1 for small frequencies and increases as the resonant frequency is approached. Around ω_0 , anomalous dispersion where the index of refraction decreases with increasing frequency occurs. Normal dispersion occurs at all other frequencies where the index of refraction increases as the frequency increases [29].

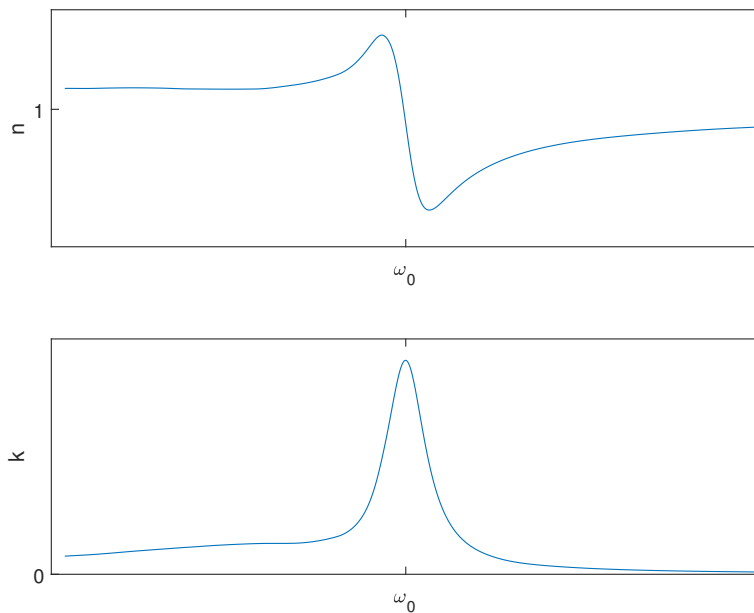


Figure 2.1: Graphs of the index of refraction (top) and the extinction coefficient (bottom) near a resonance at ω_0 .

2.4.2. Conducting Media

The effects of conduction on a propagating electromagnetic wave can be treated similarly to how the effects of polarization were modeled in Section 2.4.1. In a conducting medium, the electrons are no longer bound to their atoms, eliminating the elastic restoring force, and resulting in an equation of motion

$$m \frac{d\vec{v}}{dt} + m\tau^{-1}\vec{v} = -e\vec{E}, \quad (2.44)$$

where \vec{v} is the velocity of the electron, and $m\tau^{-1}$ is the frictional dissipation constant. Using the equation for current density

$$\vec{J} = -Ne\vec{v}, \quad (2.45)$$

where N is the number of electrons per unit volume, Equation 2.44 can be rewritten as

$$\frac{d\vec{J}}{dt} + \tau^{-1}\vec{J} = \frac{Ne^2}{m}\vec{E}. \quad (2.46)$$

Additionally, the decay of a transient current can be described as a homogeneous equation

$$\frac{d\vec{J}}{dt} + \tau^{-1}\vec{J} = 0, \quad (2.47)$$

whose solution is $\vec{J} = \vec{J}_0 e^{-t/\tau}$. After a time of 5τ , the current can be considered to have decayed to a negligible value. For a static electric field, Equation 2.46 becomes

$$\tau^{-1}\vec{J} = \frac{Ne^2}{m}\vec{E}, \quad (2.48)$$

and the static conductivity σ will be given by

$$\sigma = \frac{Ne^2}{m}\tau. \quad (2.49)$$

Assume a harmonic time dependence for the electric field \vec{E} and the current density \vec{J} that varies as $e^{-i\omega t}$. The equation of motion will then become

$$(-i\omega + \tau^{-1})\vec{J} = \frac{Ne^2}{m}\vec{E} = \tau^{-1}\sigma\vec{E}. \quad (2.50)$$

When Equation 2.50 is solved for \vec{J} , it yields

$$\vec{J} = \frac{\sigma}{1 - i\omega\tau} \vec{E}. \quad (2.51)$$

When $\omega = 0$, the equation reduces to the static case $\vec{J} = \sigma \vec{E}$.

Substituting the expression for \vec{J} into the wave equation (Equation 2.19) gives

$$\vec{\nabla}^2 \vec{E} = \frac{1}{c^2} \frac{\partial^2 \vec{E}}{\partial t^2} + \frac{\mu_0 \sigma}{1 - i\omega\tau} \frac{\partial \vec{E}}{\partial t}. \quad (2.52)$$

A simple homogeneous plane wave solution of the form

$$\vec{E} = \vec{E}_0 e^{i(\mathcal{K}z - \omega t)} \quad (2.53)$$

is taken as the trial solution with \mathcal{K} complex as described in Equation 2.35. Therefore, it can be found that \mathcal{K} must satisfy the relation

$$\mathcal{K}^2 = \frac{\omega^2}{c^2} + \frac{i\omega\mu_0\sigma}{1 - i\omega\tau}. \quad (2.54)$$

which at low frequencies reduces to

$$\mathcal{K}^2 \approx i\omega\mu_0\sigma \quad (2.55)$$

so that $\mathcal{K} \approx \sqrt{i\omega\mu_0\sigma} = (1 + i)\sqrt{\omega\mu_0\sigma/2}$. The real and imaginary parts of \mathcal{K} are approximately equal and are given by

$$k \approx \alpha \approx \sqrt{\frac{\omega\sigma\mu_0}{2}}. \quad (2.56)$$

The real and imaginary parts of the complex index of refraction \mathcal{N} are similarly equal and can be described by

$$n \approx k \approx \sqrt{\frac{\sigma}{2\omega\epsilon_0}}. \quad (2.57)$$

The distance at which the amplitude of the wave decays to e^{-1} is known as the skin depth δ and is given by

$$\delta = \frac{1}{\alpha} = \sqrt{\frac{2}{\omega\sigma\mu_0}} = \sqrt{\frac{\lambda_0}{c\pi\sigma\mu_0}}, \quad (2.58)$$

where λ_0 is the vacuum wavelength. Equation 2.54 can be rewritten in terms of the complex index of refraction as

$$\mathcal{N}^2 = 1 - \frac{\omega_p^2}{\omega^2 + i\omega\tau^{-1}}, \quad (2.59)$$

where ω_p is the plasma frequency defined as

$$\omega_p = \sqrt{\frac{Ne^2}{m\epsilon_0}} = \sqrt{\frac{\mu_0\sigma c^2}{\tau}}. \quad (2.60)$$

Equation 2.59 is known as the Drude model. It assumes that the electrons are free within the metal and models them as a classical gas. The Drude model does not account for quantum behavior and is therefore unable to explain all properties of a metal such as the thermoelectric effect. However, it does provide a reasonable approximation of the optical constants n and k . By equating the real and imaginary parts of Equation 2.59, the following equations can be found as

$$n^2 - k^2 = 1 - \frac{\omega_p^2}{\omega^2 + \tau^{-2}}, \quad (2.61a)$$

$$2nk = \frac{\omega_p^2}{\omega^2 + \tau^{-2}} \left(\frac{1}{\omega\tau} \right), \quad (2.61b)$$

from which n and k can be extracted. It is difficult to solve for n and k analytically, and so numerical methods are typically used.

Figure 2.2 shows n and k with respect to ω . As can be seen from this graph, the refractive index n becomes less than one in the region around the plasma frequency. The extinction coefficient k has relatively high values at low frequencies and decreases monotonically as frequency increases. This results in a material that is opaque roughly below the plasma frequency and transparent above it. Good agreement is obtained for this model and empirical measurements of the alkali metals, coinage metals, in addition to several other good conductors [29].

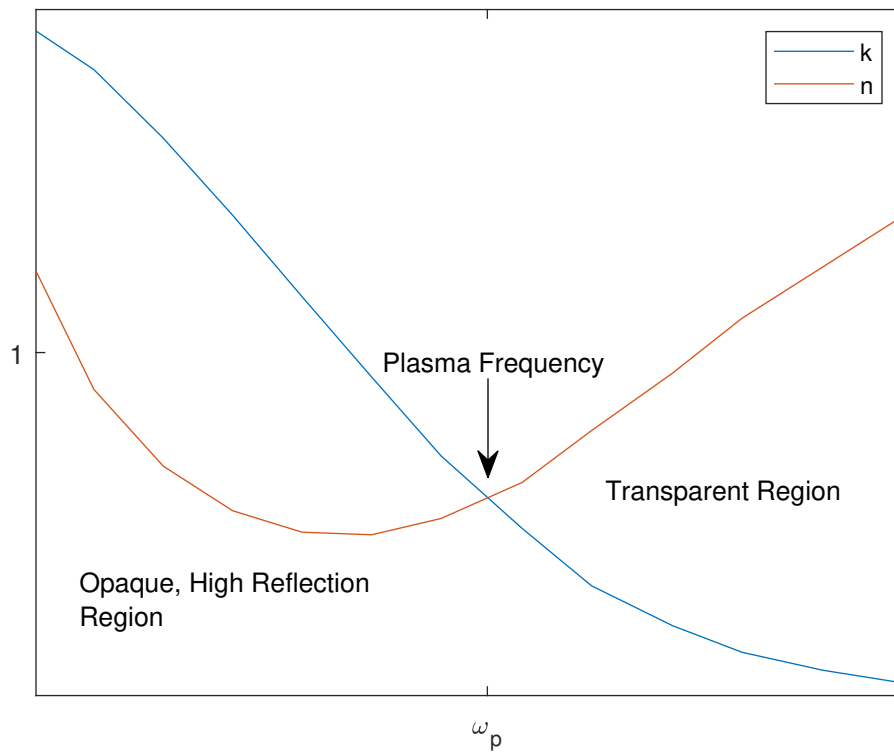


Figure 2.2: Index of refraction plotted versus frequency for a metal. Reproduced from [29]

2.4.3. Anisotropic Media

Materials which have different optical properties in different propagation directions and optical polarizations are called anisotropic media. All optical materials can be described as one of the following types:

Single crystalline: Materials whose molecules exhibit perfect periodicity along the entire dielectric and are orientated in a same direction are called single crystalline. They have the lowest energy state and are mainly anisotropic.

Polycrystalline (Non-Crystalline): These solids have long-range order, but there are boundaries that impede continuity along the long-range ordering. Polycrystalline materials can be thought of as a collection of randomly assorted grains. In general, each of the grains is anisotropic, but their averaged macroscopic behavior is isotropic.

Amorphous: These solids do not have any long-range order, and their molecules are randomly oriented. As a result, their energy state is higher than for a crystalline solid. In general, amorphous solids are anisotropic with an isotropic averaged macroscopic behavior [31, 32].

The induced polarization in an isotropic medium is related to the electric field by a parallel scalar factor, which does not have any relation to the direction of the applied electric field. However, for anisotropic media, the magnitude and direction of polarization depends on the direction of \vec{E} . In the case of linear anisotropic media with a dielectric permittivity tensor ϵ_{ij} the electric flux density is given by

$$\begin{aligned} D_x &= \epsilon_{11}E_x + \epsilon_{12}E_y + \epsilon_{13}E_z, \\ D_y &= \epsilon_{21}E_x + \epsilon_{22}E_y + \epsilon_{23}E_z, \\ D_z &= \epsilon_{31}E_x + \epsilon_{32}E_y + \epsilon_{33}E_z, \end{aligned} \tag{2.62}$$

where $i, j = 1, 2, 3$ denote the x, y, z component of coordinate system, respectively. This equation

can be rewritten using tensor notation as

$$D_i = \varepsilon_{ij}E_j. \quad (2.63)$$

If the coordinate system is chosen so that the off-diagonal elements of the tensor ε_{ij} are zero, then Equation 2.62 becomes

$$D_x = \varepsilon_x E_x, \quad D_y = \varepsilon_y E_y, \quad D_z = \varepsilon_z E_z, \quad (2.64)$$

where the 11, 22, and 33 subscripts are rewritten as x , y , and z , respectively. The index of refraction is related to the dielectric and magnetic constants as

$$n^2 = \varepsilon_r \mu_r = \begin{bmatrix} \varepsilon_x & 0 & 0 \\ 0 & \varepsilon_y & 0 \\ 0 & 0 & \varepsilon_z \end{bmatrix} \begin{bmatrix} \mu_x & 0 & 0 \\ 0 & \mu_y & 0 \\ 0 & 0 & \mu_z \end{bmatrix} = \begin{bmatrix} n_x^2 & 0 & 0 \\ 0 & n_y^2 & 0 \\ 0 & 0 & n_z^2 \end{bmatrix}. \quad (2.65)$$

Assuming non-magnetic media ($\mu_r = 1$), the relation between these permittivities and corresponding refractive indices can be rewritten as

$$n_i^2 = \varepsilon_i / \varepsilon_0. \quad (2.66)$$

If the dielectric permittivity tensor ε_{ij}^{-1} is inverted and multiplied with ε_0 , the electric field then becomes

$$\varepsilon_0 \vec{E} = \varepsilon_0 (\varepsilon_{ij}^{-1}) \vec{D}, \quad (2.67)$$

which can also be written as

$$\varepsilon_0 \vec{E} = \vec{\eta} \vec{D}, \quad (2.68)$$

where $\vec{\eta} = \varepsilon_0 (\varepsilon_{ij}^{-1})$ is the impermeability tensor. Due to the symmetry of ε , this tensor is diagonal with Equation 2.66 valid. If $\vec{\eta}$ is rewritten in quadratic form, the index ellipsoid can be obtained as

$$\eta_{ij} x_i x_j = 1, \quad i, j = 1, 2, 3. \quad (2.69)$$

If the principle axes x , y , and z are chosen to be the coordinate system, the index ellipsoid can then be written

$$\frac{x^2}{n_x^2} + \frac{y^2}{n_y^2} + \frac{z^2}{n_z^2} = 1, \quad (2.70)$$

where n_x , n_y , and n_z are the principal refractive indices.

Based on the index ellipsoid equation Equation 2.70, there are three cases for the optical symmetry of a material:

1. Isotropic—All three principal refractive indices are equal ($n_x = n_y = n_z$)
2. Uniaxial —Two of the principal indices are equal ($n_x = n_y \neq n_z$)
3. Biaxial —None of the principal indices are equal ($n_x \neq n_y \neq n_z$)

2.5. The Mueller Matrix

The Mueller matrix is a 4x4 matrix that completely specifies the interaction of light with a specular sample, and can describe polarized, partially polarized, and unpolarized light [33]. Incoming and outgoing beams are specified by their Stokes vectors. For an isotropic sample, the Mueller matrix is given by

$$M_{isotropic} = \begin{bmatrix} 1 & -N & 0 & 0 \\ -N & 1 & 0 & 0 \\ 0 & 0 & C & S \\ 0 & 0 & -S & C \end{bmatrix}, \quad (2.71)$$

where

$$N = \cos(2\Psi), \quad (2.72a)$$

$$C = \sin(2\Psi)\cos(\Delta), \quad (2.72b)$$

$$S = \sin(2\Psi)\sin(\Delta), \quad (2.72c)$$

and Ψ and Δ are the standard ellipsometer angles. For an anisotropic sample, the matrix becomes

$$M_{anisotropic} = \begin{bmatrix} 1 & -N - \alpha_{ps} & C_{sp} + \zeta_1 & S_{sp} + \zeta_2 \\ -N - \alpha_{sp} & 1 - \alpha_{sp} - \alpha_{ps} & -C_{sp} + \zeta_1 & S_{sp} + \zeta_2 \\ C_{ps} + \xi_1 & -C_{ps} + \xi_1 & C + \beta_1 & S + \beta_2 \\ -S_{ps} + \xi_2 & S_{ps} + \xi_2 & -S + \beta_2 & C - \beta_1 \end{bmatrix}, \quad (2.73)$$

where

$$D = \frac{2}{1+N}, \quad (2.74a)$$

$$\zeta_1 = (D/2)(CC_{ps} + SS_{ps}), \quad (2.74b)$$

$$\zeta_2 = (D/2)(CS_{ps} + SC_{ps}), \quad (2.74c)$$

$$\xi_1 = (D/2)(CC_{sp} + SS_{sp}), \quad (2.74d)$$

$$\xi_2 = (D/2)(CS_{sp} + SC_{sp}), \quad (2.74e)$$

the α and β terms are second order, off-diagonal elements of the Jones matrix that can be neglected and the subscripts, p and s refer to the two polarization modes [34]. The normalization condition is given by

$$N^2 + S^2 + C^2 + S_{sp}^2 + C_{sp}^2 + S_{ps}^2 + C_{ps}^2 = 1. \quad (2.75)$$

Depolarization can be introduced by variation of film thickness over the incident beam size [35], quasi-monochromatic light, and back reflections [36]. For this case, the Mueller matrix is charac-

terized by a general normalized Mueller matrix added to a total depolarizer

$$M_{anisotropic,depolarizing} = \begin{bmatrix} 1 & m_{01} & m_{02} & m_{02} \\ m_{10} & m_{11} & m_{12} & m_{12} \\ m_{20} & m_{21} & m_{22} & m_{22} \\ m_{30} & m_{31} & m_{32} & m_{32} \end{bmatrix} + (1-p) \begin{bmatrix} 1 & 0 & 0 & 0 \\ 0 & 0 & 0 & 0 \\ 0 & 0 & 0 & 0 \\ 0 & 0 & 0 & 0 \end{bmatrix}, \quad (2.76)$$

where $m_{i,j}$ are the matrix elements in Equation 2.73 and p is the fraction of polarized light. The normalization condition is now

$$N^2 + S^2 + C^2 + S_{sp}^2 + C_{sp}^2 + S_{ps}^2 + C_{ps}^2 = p^2. \quad (2.77)$$

2.6. The Hyperbolic Dispersion Relation

As obtained in crystal optics [37], the relative permittivity of a material can be described in Cartesian coordinates using the diagonalized tensor:

$$\epsilon_r = \begin{bmatrix} \epsilon_{xx} & 0 & 0 \\ 0 & \epsilon_{yy} & 0 \\ 0 & 0 & \epsilon_{zz} \end{bmatrix}. \quad (2.78)$$

For an isotropic material,

$$\epsilon_{xx} = \epsilon_{yy} = \epsilon_{zz}, \quad (2.79)$$

and for a uniaxial material,

$$\epsilon_{xx} = \epsilon_{yy} \neq \epsilon_{zz}. \quad (2.80)$$

Most hyperbolic metamaterials are uniaxial [38]. For a type-I hyperbolic metamaterial, $\epsilon_{xx} > 0$ and $\epsilon_{zz} < 0$ whereas a type-II HMM has $\epsilon_{xx} < 0$ and $\epsilon_{zz} > 0$ [4].

The constitutive relations connecting the electric displacement \vec{D} and the magnetic induction \vec{B} to the electric and magnetic fields \vec{E} and \vec{H} can be written as

$$\vec{D} = \epsilon_0 \epsilon_r \vec{E}, \quad (2.81)$$

$$\vec{B} = \mu_0 \mu_r \vec{H}. \quad (2.82)$$

The dispersion relation for a uniaxial HMM can be calculated from the following versions of Faraday's Law and the Ampère-Maxwell Law:

$$\frac{\partial \vec{B}}{\partial t} = -\vec{\nabla} \times \vec{E}. \quad (2.83)$$

$$\frac{\partial \vec{D}}{\partial t} = \vec{\nabla} \times \vec{H}, \quad (2.84)$$

Assuming a plane wave with the expressions $\vec{E} = \vec{E}_0 e^{i(\omega t - k \cdot r)}$ and $\vec{H} = \vec{H}_0 e^{i(\omega t - k \cdot r)}$, the above equations simplify to

$$k \times \vec{E} = \omega \mu_0 \vec{H}, \quad (2.85)$$

$$k \times \vec{H} = -\omega \epsilon_0 \epsilon_r \vec{E}. \quad (2.86)$$

Substitution of the above equations into the wave equation (Equation 2.19) leads to the eigenvalue equation for the electric field \vec{E}

$$k \times (k \times \vec{E}) + \omega^2 \mu_0 \epsilon_0 \epsilon_r \vec{E} = 0, \quad (2.87)$$

which can be developed in matrix form as

$$\begin{bmatrix} k_0^2 \epsilon_{xx} - k_y^2 - k_z^2 & k_x k_y & k_x k_z \\ k_y k_x & k_0^2 \epsilon_{yy} - k_x^2 - k_z^2 & k_y k_z \\ k_z k_x & k_z k_y & k_0^2 \epsilon_{zz} - k_x^2 - k_y^2 \end{bmatrix} \begin{bmatrix} \vec{E}_x \\ \vec{E}_y \\ \vec{E}_z \end{bmatrix} = 0, \quad (2.88)$$

where k_x , k_y , and k_z are the respective x, y, and z components of the wave vector, $k_0 = \frac{\omega}{c}$ is the vacuum wave number, and $c = 1/\sqrt{\epsilon_0\mu_0}$ is the speed of light in vacuum. Assuming uniaxial hyperbolic media, and ignoring trivial solutions, the final dispersion relation is given as

$$\frac{k_x^2 + k_y^2}{\epsilon_{zz}} + \frac{k_z^2}{\epsilon_{xx}} = \frac{\omega^2}{c^2}, \quad (2.89)$$

which is found by solving the eigenvalue problem [39].

2.7. Effective Medium Theory (EMT)

Consider media that is periodically stratified (Figure 2.3) normal to the direction of propagation. If the wavelength of light is much larger than the period of stratification, it can be approximated that either the electric field \vec{E} or the electric field displacement \vec{D} are continuous across the interfaces of the media and that

$$\epsilon_{eff} \approx \frac{\vec{D}_{av}}{\vec{E}_{av}}. \quad (2.90)$$

The field that is constant depends on the polarization of the incident light. This means that the stratified medium can be treated as two different effective bulk media for both the x/y and z directions. From Maxwell's boundary conditions, the tangential component of the \vec{E} is constant at the interface between two dielectrics. For the x and y directions, an average \vec{D} can be assumed, leading to the equation for \vec{D}_{av} as

$$\vec{D}_{av} = f\vec{D}_1 + (1-f)\vec{D}_2, \quad (2.91)$$

where f is the fill factor of metal to dielectric. By contrast, the normal component of \vec{D} is continuous at material boundaries. Therefore, for the z direction, by considering an average \vec{E} , the same

constitutive relation yields a different expression for the bulk dielectric of the same structure as

$$\begin{aligned}\vec{E}_{av} &= f\vec{E}_1 + (1-f)\vec{E}_2, \\ &= f\vec{D}_0/\epsilon_1 + (1-f)\vec{D}_0/\epsilon_2.\end{aligned}\tag{2.92}$$

This kind of birefringence that occurs with subwavelength-scale structuring of isotropic material is called form birefringence [40].

This is known as zero-order EMT where the effective permittivities do not have any dependence on period [41]. Higher-order effective medium theories exist but are much more complicated without giving much more physical insight [42].

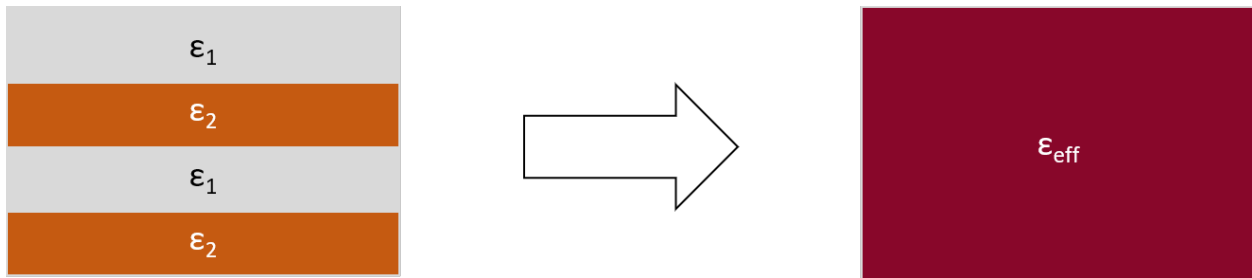


Figure 2.3: Periodically stratified media (left) can be approximated as a single, homogeneous material (right) if the period of stratification is much less than the wavelength of incident light.

Sub-wavelength inclusion of metals in a dielectric can be represented as

$$f \frac{\epsilon_m - \epsilon_{eff}}{\epsilon_m + \kappa \epsilon_{eff}} + (1-f) \frac{\epsilon_d - \epsilon_{eff}}{\epsilon_d + \kappa \epsilon_{eff}} = 0,\tag{2.93}$$

where ϵ_M is the permittivity of the metal, and ϵ_D is the permittivity of the dielectric, and κ is the screening factor related to the Lorentz polarization factor q as $\kappa = (1-q)/q$. The Lorentz polarization factor for an ellipsoid of semiaxis a_i , a_j , and a_k is given by

$$q_i = \int_0^\infty \frac{a_i a_j a_k ds}{2(s + a_a^2)^{3/2} (s + a_j^2)^{1/2} (s + a_k^2)^{1/2}},\tag{2.94}$$

where s is the surface of integration [43]. Equation 2.93 can be simplified by approximating $\kappa \gg 1$ for the in-plane direction and $\kappa \approx 0$ for the out-of-plane direction (Figure 2.4). This yields the Maxwell-Garnett EMT, resulting in the components of permittivity as follows: [44, 45]

$$\epsilon_{xx} = \epsilon_{yy} = f\epsilon_M + (1-f)\epsilon_D, \quad (2.95a)$$

$$\frac{1}{\epsilon_{zz}} = \frac{f}{\epsilon_M} + \frac{1-f}{\epsilon_D}. \quad (2.95b)$$

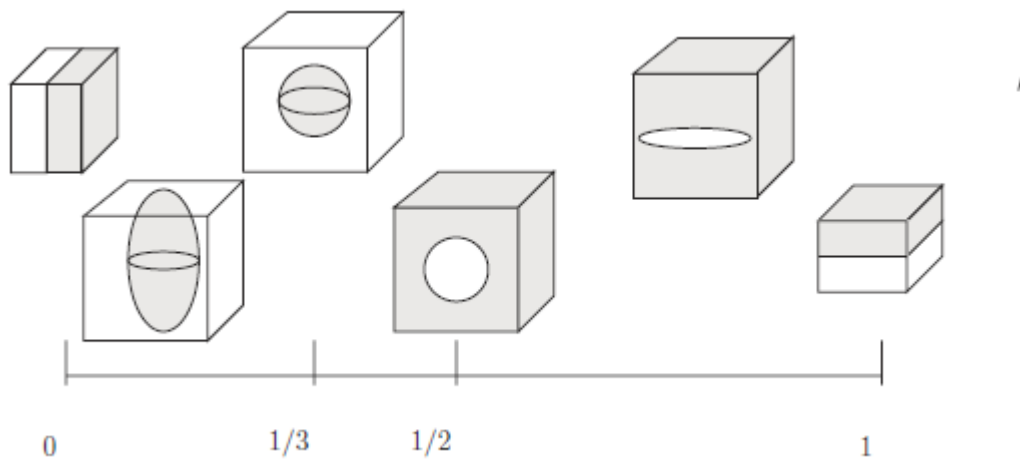


Figure 2.4: Screening factor κ for several different arrangements of binary composites. The arrow indicates the direction of incident light. Taken from [46].

3. DESIGN AND EFFECTIVE OPTICAL BEHAVIOR

3.1. HMM with ENZ near 633 nm

The first designed device was an HMM with the ENZ region near the He-Ne wavelength of 633 nm. This wavelength was chosen as the ENZ region because of the wide availability of components for that wavelength and the resulting ease of characterization. The first step in the design was to determine the materials and the desired optical behavior. Copper and titanium dioxide were chosen due to the low cost and ease of fabrication of both materials. The values of the optical constants for the materials were obtained from the relevant literature [47, 48] for the initial design. Figure 3.1 shows a log plot of the magnitude of the real part of permittivity in the z direction based on EMT calculations. The ENZ lines [49] are marked with the red arrows in Figure 3.1. As the fill factor increases, the magnitude of the resonant response in the imaginary part of permittivity also increases. A fill factor of 67% where the Cu thickness is double the TiO₂ thickness was determined to have the ENZ closest to 633 nm. The 67% fill factor is marked with a red arrow on the y axes of the surface plots. The red ellipse shows the ENZ for this fill factor. The HMM designed in this paper shows a type-II uniaxial response. Figure 3.2 shows the permittivity response for this design in all directions. The z direction acts like a dielectric, with an antiresonant response in the real part of permittivity and a resonant response around the ENZ region in the imaginary part. In contrast, the x and y directions act like a metal (see Section 2.4.2), having a negative real part of permittivity and a small positive imaginary part. Finally, the isofrequency curve at 633 nm, calculated with the EMT values inserted in Equation 2.89, is shown in Figure 3.3.

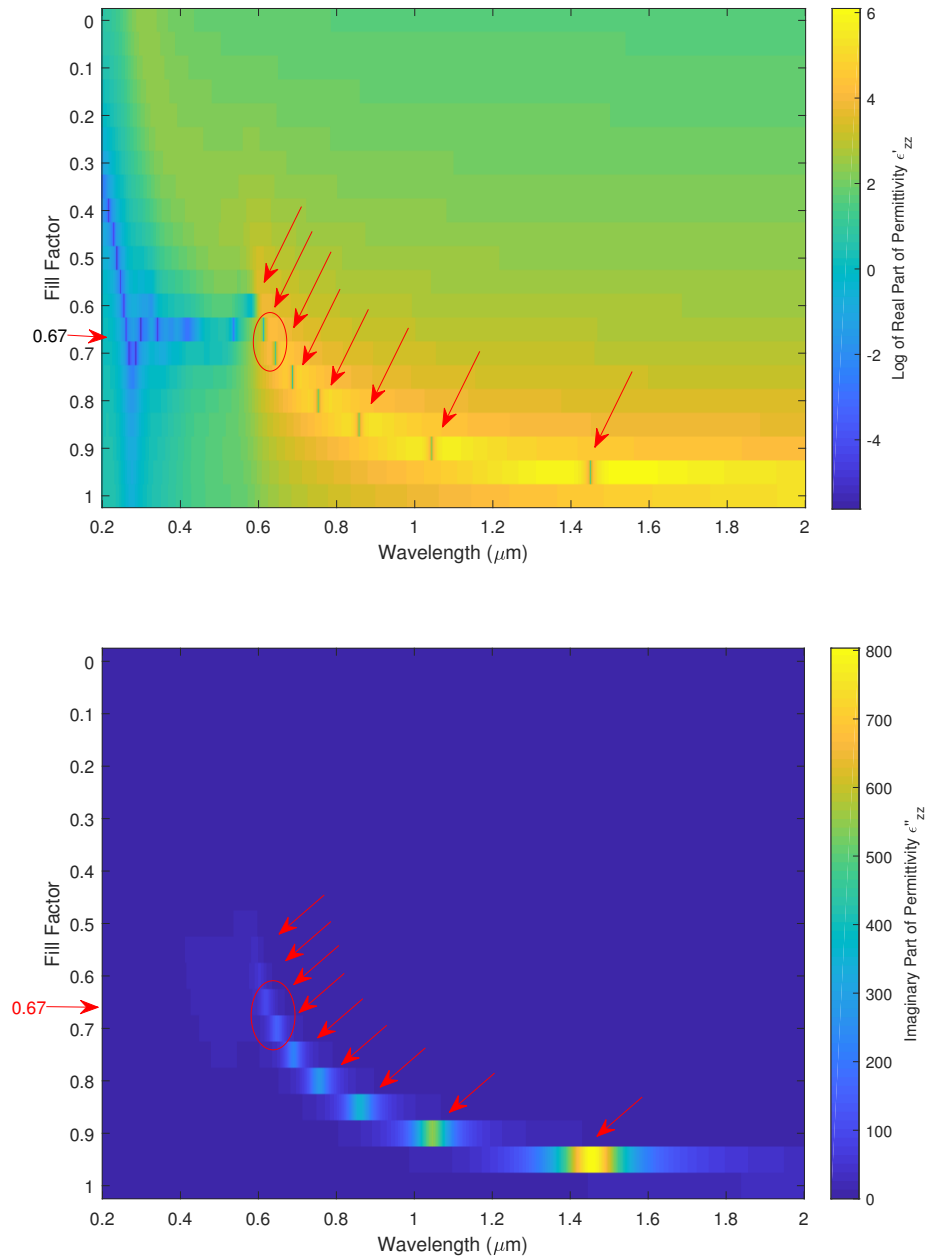


Figure 3.1: The response in the z direction of the HMM with respect to wavelength and fill factor. The red arrows show the ENZ region, and the ellipses show the ENZ region occurring near the He-Ne wavelength at a fill factor of 67%.

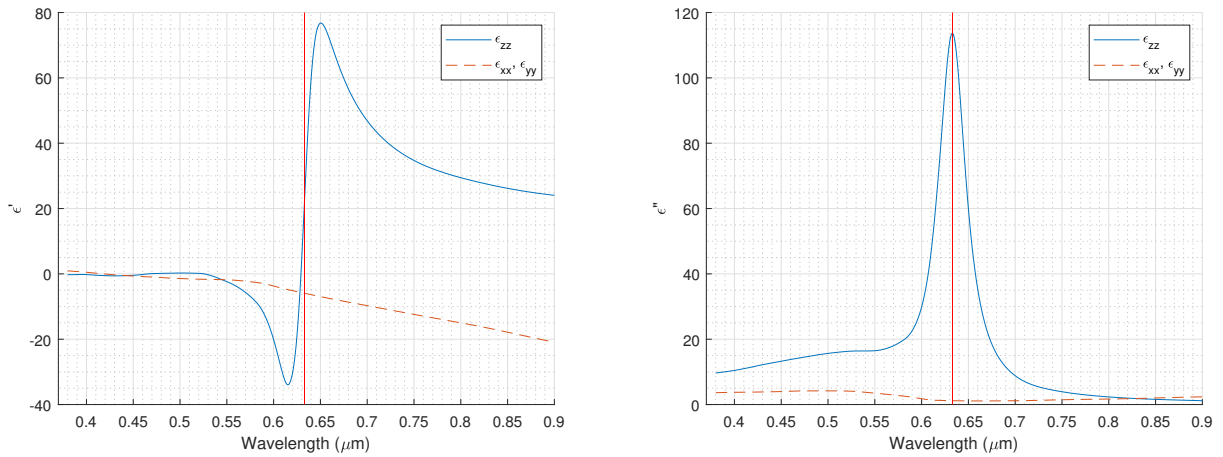


Figure 3.2: The expected electrical permittivity of the designed HMM. The solid line represents the z direction whereas the dotted line represents the x and y directions. The ENZ is intentionally placed near the He-Ne wavelength of 633 nm. The He-Ne line is shown as the red vertical line.

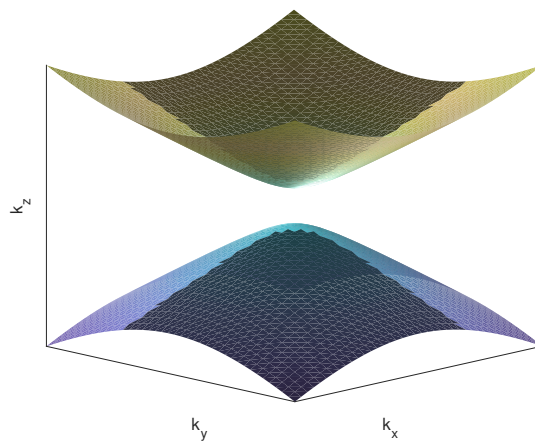


Figure 3.3: The isofrequency curve for the Cu/TiO₂ at 633 nm calculated with EMT permittivity values.



Figure 3.4: Cross-section of the final 15 nm Cu/TiO₂ design. Devices with periods of 20 nm were also made with the same fill factor. This device produces an ENZ line at, and is hyperbolic above, the He-Ne wavelength of 633 nm.

3.2. Al/TiO₂ HMM

In order to verify the ellipsometric measurement process (Section 4.2.1), a second HMM design was made using Al and TiO₂. The device was designed to have hyperbolic dispersion at wavelengths above the He-Ne wavelength of 633 nm. Experimentally measured values from the relevant literature were again used for the optical constants [48, 50]. Figure 3.6 shows a log plot of magnitude of the real part of permittivity in the z direction based on EMT calculations. As the fill factor increases, the antiresonant response in the real part of permittivity also increases. A fill factor of 90% where the Cu thickness is ninefold greater than the TiO₂ thickness was determined to have material polarization resonance in the visible wavelengths. The HMM designed again shows a type-II uniaxial response. Figures 3.5 and 3.7 show the complete permittivity response for this design. The z direction acts like a dielectric, with an antiresonant response in the real part of permittivity and a resonant response around the ENZ region in the imaginary part. In contrast, the x and y directions act like a metal, having a negative real part of permittivity and a small positive imaginary part.

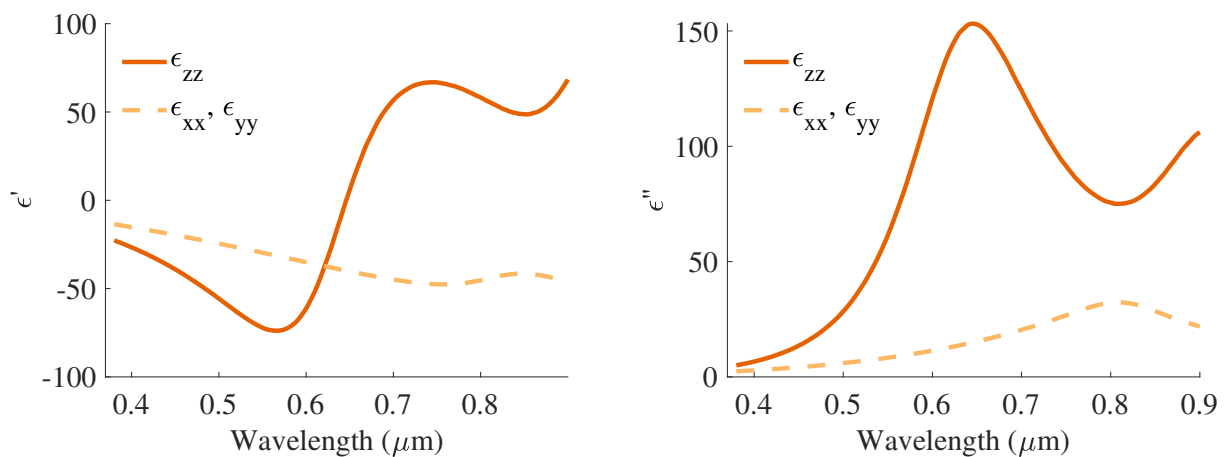


Figure 3.5: The expected permittivity for a Al/TiO₂ HMM

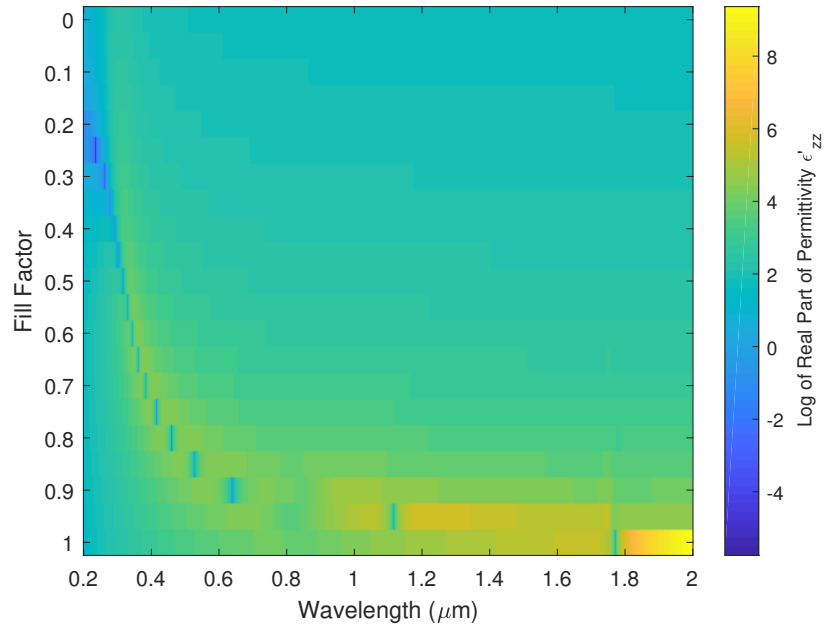


Figure 3.6: The ϵ'_z response of the Al/TiO₂ HMM with respect to wavelength and fill factor.

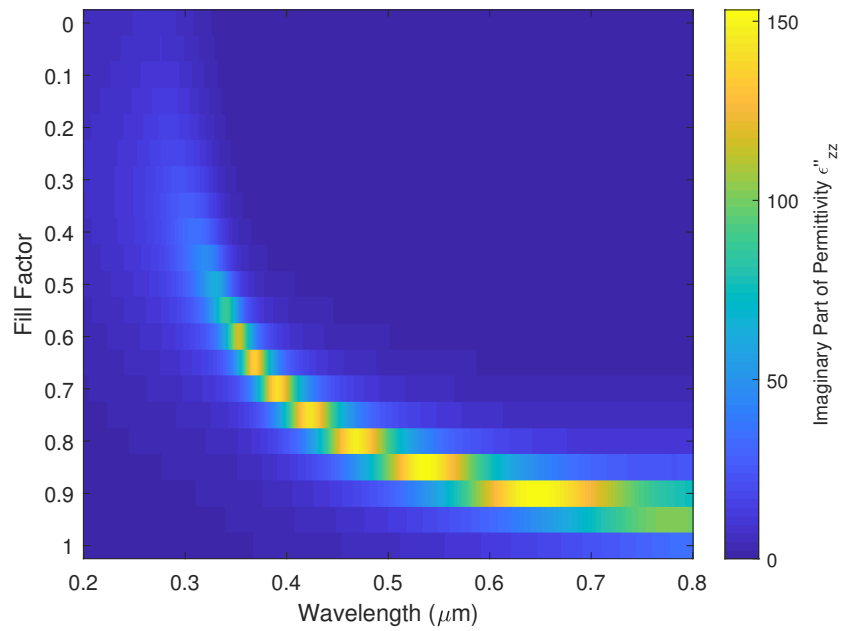


Figure 3.7: The ϵ''_z response of the Al/TiO₂ HMM with respect to wavelength and fill factor.

3.3. Biaxial HMM

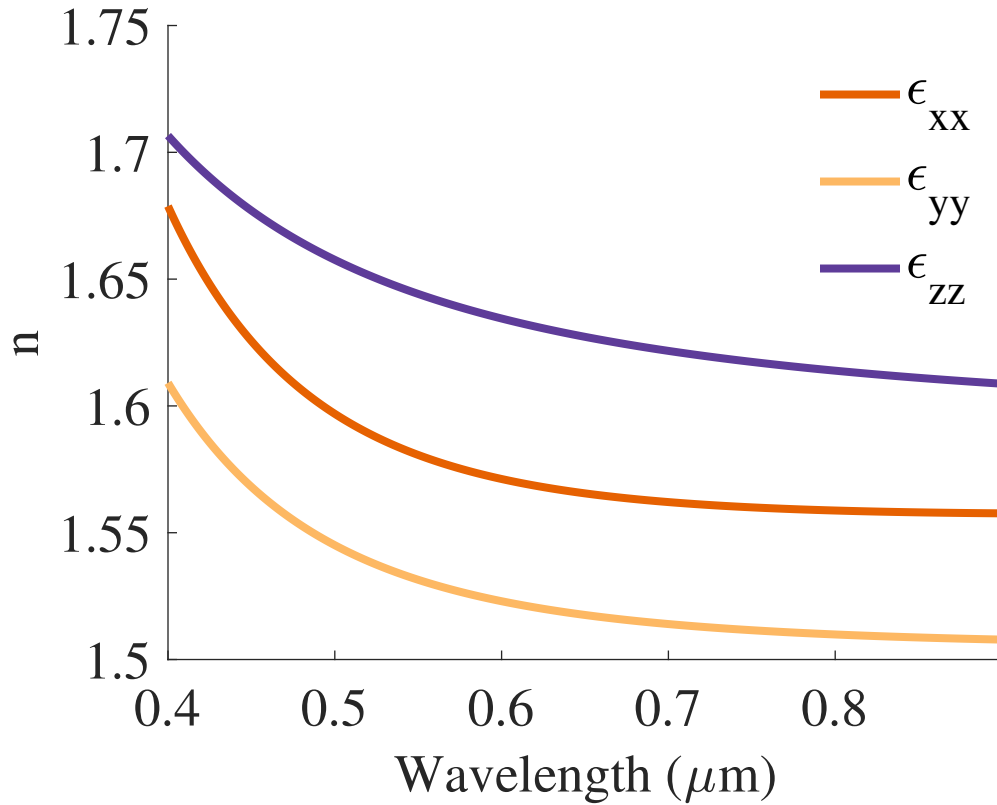


Figure 3.8: The indices of refraction for OAD deposited TiO_2

As described in Section 2.6, most of the HMMs produced have been uniaxial, with the x and y directions having the same optical behavior. Producing a biaxial HMM would allow for all three Cartesian directions to be engineered, enabling several promising research applications [38]. It would be possible to produce a biaxial HMM by either patterning the isotropic multilayers to be different in the x and y directions or by depositing optically biaxial films.

Thin films with an optically biaxial response can be produced using a technique known as oblique angle deposition (OAD). In conventional depositions, the substrate is oriented parallel to the base of the source crucible. As long as the distance is less than the mean free path of the chamber, the

evaporated material will condense on the surface to form a flat, even layer. The condensation of the material shadowing occurs as microscopic nuclei. However, in the case of OAD, the substrate is intentionally tilted with respect to the source crucible. The ballistic shadowing that occurs due to the small nuclei causes nano-wires to grow on the surface. The nano-wires are tilted towards the deposition source, and have a biaxial orientation [51–54]. The Cauchy values for TiO_2 deposited using the MiNDS facility were obtained from [55] and are shown in Figure 3.8. In this design, the tilt angle α was set to be 70° .

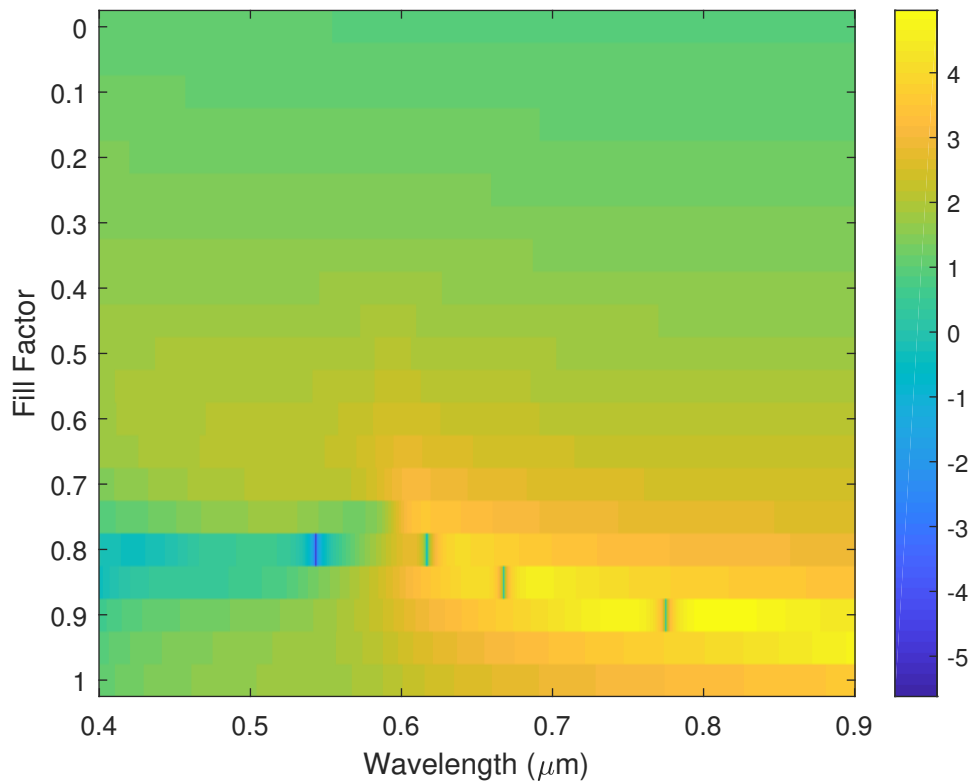


Figure 3.9: The surface plot for a biaxial Cu/ TiO_2 metamaterial. The color bar represents the base-ten logarithm of the real part of the out-of-plane permittivity ϵ'_{zz} .

Again, this device was designed to have its ENZ response near the He-Ne wavelength of 633 nm. Copper and titanium dioxide were again chosen to be the respective metal and dielectric due

to their low cost, ease of fabrication, and familiarity. For more information on how the EMT calculations were performed for a biaxial material, see Appendices A.2 and A.4.

Figure 3.9 shows a log plot of magnitude of the real part of permittivity in the z direction based on EMT calculations. As the fill factor increases, the magnitude of the antiresonant response in the real part of permittivity also increases. A fill factor of 80% where the Cu thickness is quadruple the TiO₂ thickness was determined to have the ENZ closest to 633 nm. The HMM designed shows a type-II biaxial response. Figure 3.10 shows the complete permittivity response for this design. The z direction acts like a dielectric, with an antiresonant response in the real part of permittivity and a resonant response around the ENZ region in the imaginary part. In contrast, the x and y directions act like a metal, having a negative real part of permittivity and a small positive imaginary part. Figure 3.11 shows a magnified view of the region where all three permittivities meet, showing the biaxial response. While there is not a large change in index between n_x and n_y , this is similar to other anisotropic materials. For example, quartz has a birefringence of 0.005 at 633 nm [56]. The biaxial response could be increased by decreasing the fill factor so there would be a larger proportion of TiO₂. However, this would shift the ENZ region so it would no longer be around 633 nm. This device was not fabricated due to time constraints.

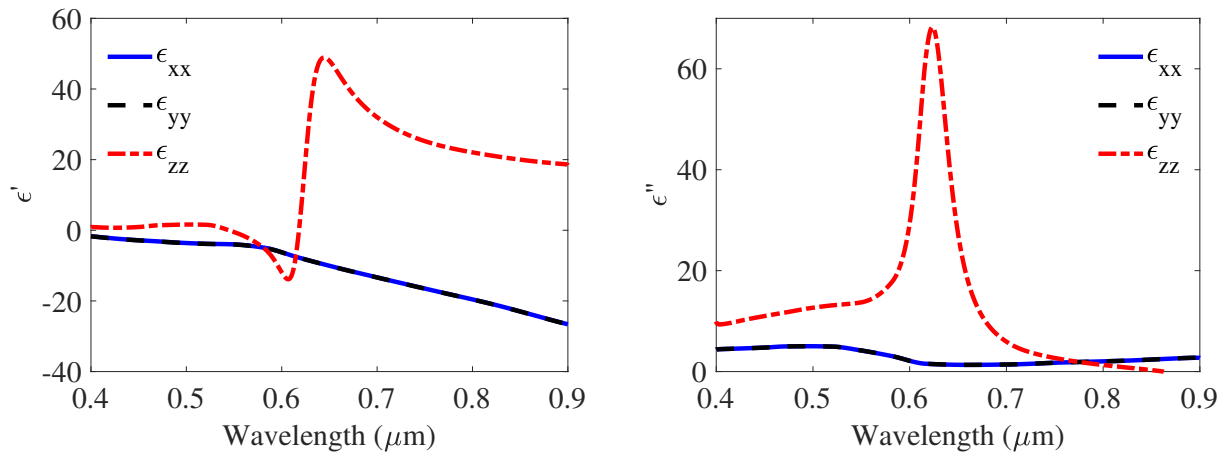


Figure 3.10: The expected electrical permittivity of the designed biaxial HMM. The real part of permittivity is shown on the left whereas the imaginary part is shown on the right.

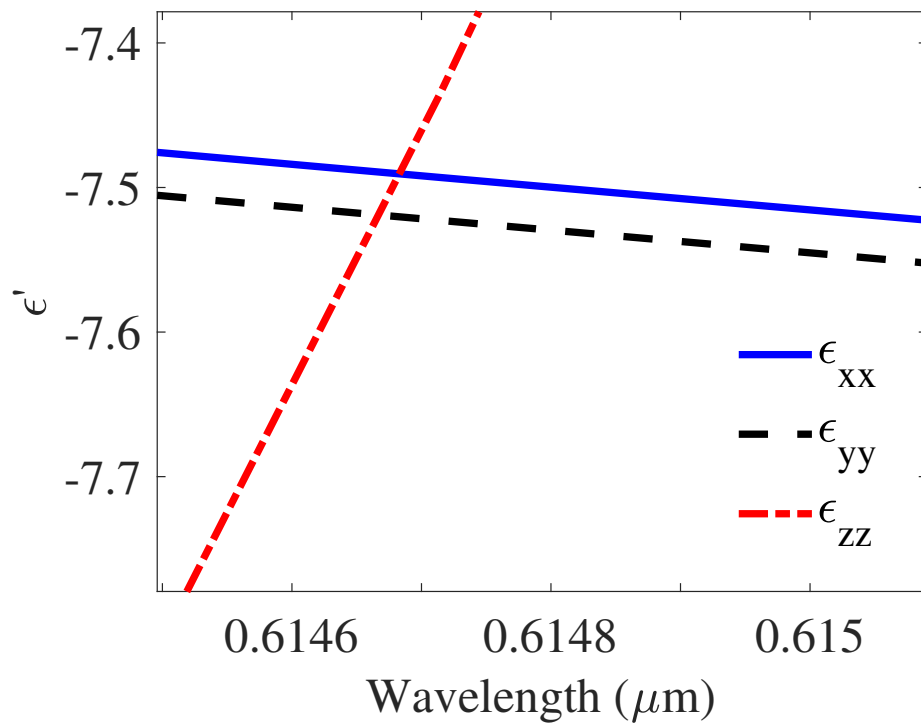


Figure 3.11: A zoomed-in view of the biaxial HMM around the point where the three permittivities meet showing the biaxial behavior of the device.

3.4. Cu/Air HMM

Using OAD, it is possible to fabricate nanowires of copper [57, 58]. The combination of Cu and the dielectric air surrounding these nanowires should act like an HMM.

Calculations using EMT were performed to determine the expected behavior of this subwavelength combination of air and Cu. It was assumed that the fill factor of Cu and air would be around 50% and that the device would have a uniaxial response. While the fabricated device was actually be biaxial, the small difference between the x and y directions allowed this assumption to be made.

The results from the EMT calculations are shown in Figure 3.12. The z direction acts like a dielectric with a positive permittivity. In contrast, the x and y directions act like a metal, having a negative real part of permittivity and a small positive imaginary part. It should be noted that this device has a hyperbolic response across the entire visible spectrum.

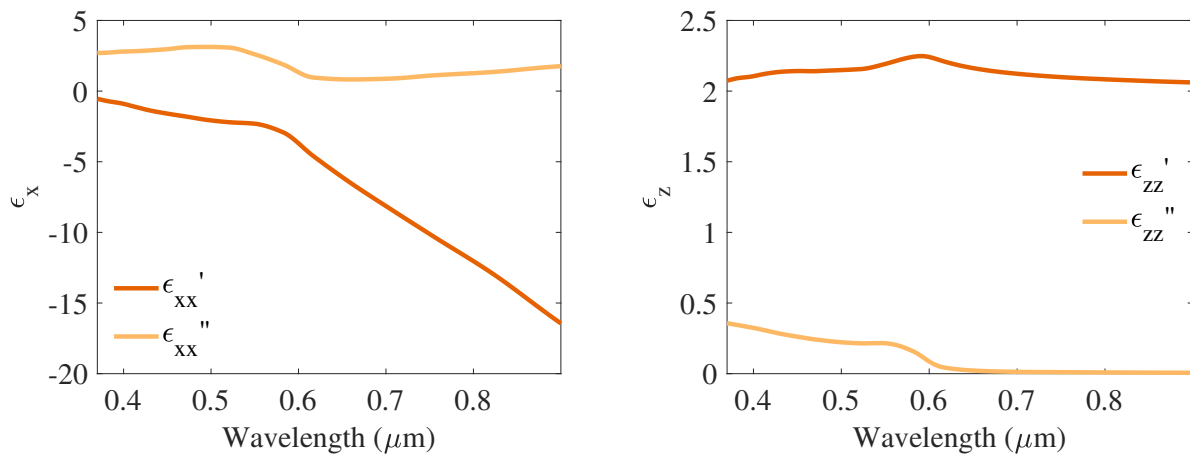


Figure 3.12: The expected electrical permittivity of the OAD deposited Cu. The permittivity for the x and y directions is shown on the left whereas the permittivity for the z direction is shown on the right. Notice that the this device is showing hyperbolic dispersion with a positive ϵ'_z and a negative ϵ'_x .

4. FABRICATION AND CHARACTERIZATION

4.1. Fabrication

A PVD 75 electron beam deposition system from Kurt J. Lesker was used to deposit the thin films onto the substrate after it was thoroughly cleaned using hydrofluoric acid (HF) and a three solvent rinse of acetone, methanol, and isopropanol. The Cu deposition was performed at 2 Å/s, the Al deposition was performed at 5 Å/s, and the TiO₂ deposition was performed at 0.1 Å/s. The deposition rates were measured using crystal monitors to ensure that the proper ratio of materials was obtained. The tooling factor was kept the same at 90.5% for both the metal and the dielectric to ensure approximately the same error for the two materials, keeping the proper fill factors. The sample was kept under a vacuum pressure less than 2.5×10^{-5} Torr for the entire deposition process, including switching between materials.

Two different HMM implementations were used: one consisting of Cu/TiO₂ multilayers and the other consisting of Al/TiO₂ multilayers. The Cu/TiO₂ multilayers had a fill factor of 67%, meaning the Cu layers were twice as thick as the TiO₂ layers. The fabrication process was based on previous subwavelength layers deposited with PVD used to fabricate one-dimensional photonic crystals [59]. The top layer was always a dielectric to prevent oxidation. Devices had consistent ellipsometric measurements six months apart, suggesting that they are not oxidizing. The Al/TiO₂ multilayers had a period of 50 nm, and a fill factor of 90%. Additionally, copper nanowires were deposited which were expected to have a hyperbolic response. Since the periods were around $\lambda/10$, the devices could be approximated as homogeneous effective media [60].

4.1.1. Thin Film Deposition Using EB-PVD

Thin films of titanium dioxide, copper, and aluminum were used to make HMMs. Titanium (Ti) has an atomic number of 22 and makes up 0.63% of the earth's crust, making it the ninth most abundant element [61]. The naturally forming oxide of titanium is titanium dioxide, which is also called Titanium(IV) oxide or titania. Titanium dioxide exists mainly in three crystalline polymorphs: rutile (tetragonal), anatase (tetragonal), and brookite (orthorhombic). All of these three crystalline polymorphs (phases) occur naturally, with rutile being the most common [61–63]. All of the naturally occurring crystals are birefringent, with the tetragonal crystal system having a uniaxial optical symmetry and the orthorhombic crystal system having a biaxial optical symmetry [28].

Copper (Cu) has an atomic number of 29 and is one of the few metals that occurs in nature as a directly usable metal. It is malleable, ductile, and has a high thermal and electrical conductivity. It can be used as a building material, in coins, and as an alloy component [64]. Copper is low cost, but unfortunately has a higher reactivity than silver and gold.

Aluminum (Al) is considered to be the best plasmonic material for the ultraviolet (UV), but can also be used for visible applications. It has an atomic number of 13 and is widely used in the aerospace and transportation industries. Like copper, aluminum forms a passivation layer by reacting with airborne oxygen. Unfortunately, this affects the optical properties of the material, meaning that steps must be taken to prevent it from oxidizing [50]. Copper and aluminum are becoming more widely used in optics because of their plasmonic effects in the UV and visible range, and because of their compatibility in CMOS processing [65–67].

Several ways to deposit thin films exist, including chemical vapor deposition (CVD), sol-gel dip coating process, atomic layer deposition (ALD), pulsed laser deposition (PLD), and DC reactive magnetron sputtering [68–73]. Another technique for depositing optical thin films is e-beam PVD,

which produces amorphous thin films such as TiO_2 [74]. This technique was used to fabricate the HMMs in this work.

In e-beam PVD, the material is held in a crucible at the base of the chamber. A filament is used to create a source of electrons. An electric potential difference on the order of a few kilovolts is held between the e-beam source and the crucible, causing the electrons to be accelerated into the source material. This intense beam of electrons with high-energy is able to vaporize the source material, causing it to sublime onto the substrate to form a thin film. The deposition chamber should have a small enough pressure so that the mean free path of the material is greater than the distance between the crucible and the substrate [75]. For the PVD system at the MiNDS facility, this is around 7.5×10^{-5} Torr. In order to keep the beam of electrons away from the cathode source, and to guide the evaporated beam to melt the source fully, electric and magnetic fields are applied to direct the beam. In the case of TiO_2 , the material needs to be melted to release oxygen since titanium includes multiple stable oxides which need to be reduced before the main deposition [76].

For the materials used in this research, a reinfiltrated graphite crucible as shown in Figures 4.1 and 4.2 was used. The e-beam PVD model that is used for the fabrication of the device is a PVD 75 from Kurt J. Lesker Company as shown in Figure 4.3. The fill volume is important to prevent damage to the crucible liner. By overfilling the crucible, the material may wick over the side of the crucible, causing a thermal short circuit between the liner and the hearth. This will result in a higher power necessary to melt the material, eventually causing the crucible to crack. Some materials, such as aluminum, are much worse at wicking over the side of the crucible than others. It can also cause damage to have too little material inside the crucible (less than 2/3 of crucible), either by initially not using enough material or by not refilling after a deposition. If there is not enough material in the crucible, the beam of electrons will strike the crucible instead of the source

material, causing sparking. Eventually, the e-beam will crack or even melt the crucible and will cause damage to the PVD system. To avoid this damage, the amount of material was kept between $2/3$ and $3/4$ of the crucible during evaporations, and the material levels were regularly checked [76].



(a)



(b)

Figure 4.1: Crucible filled with Cu: (a) before deposition; and (b) after deposition when the Cu is melted



Figure 4.2: Crucible with TiO₂: (a) before deposition; and (b) after deposition showing the melted TiO₂ [55].



Figure 4.3: The PVD 75 used for HMM fabrication [55].

Difficulties were encountered during the TiO₂ deposition. The highest deposition rate of TiO₂ is around 3 to 5 Å/second, which makes fabrication of relatively thick layers time consuming [76]. The main problem encountered was that if the initial deposition rate was set to be high, an interlock would be triggered, and the deposition would end. Originally, it was thought that this was caused by the increased e-beam power causing electrical arcing in the chamber. However, it is more likely that this is caused by water vapor from the material surface causing a large spike in the chamber pressure. TiO₂ has 90% surface coverage at 3×10^{-8} mbar of water at a pressure of 2.25×10^{-8} Torr. At typical deposition pressures, the surface is highly likely to be fully coated with water that is then boiled off during deposition. At a higher vacuum of around 1×10^{-8} Torr, the water would dissipate in around half of an hour. The more the chamber is used to deposit TiO₂, the bigger this problem becomes as the porous film collects water, and then releases it as it is hit from the e-beam radiation [77].

This issue was avoided by raising the power slowly as the deposition continued, allowing the material time to warm up. Deposition of TiO₂ was started at a deposition rate of 0.2 Å/second and gradually increased to the maximum rate (the highest rate achieved in the MiNDS facility is around 1.2 Å/second). However, a better way to prevent this, according to Dr. Scott Kirkpatrick, would be to perform more sample heating and to try to maintain vacuum as much as possible by performing loading and unloading quickly. The recipe should be optimized to achieve this. To perform more heating, the shutter should be kept closed, and the ramp function should be used to raise and hold the deposition power. The e-beam power should be increased with a slow ramp over two minutes to a percentage that will deposit, keeping the shutter closed. Next, the power should be held for 60 seconds. Finally, there should be a ramp over two to five minutes to a higher rate than with all shutters still kept closed, with a soak time of 60 seconds. For the deposition, the

shutters should be opened with the SQS-242 software given total control.

Another problem is that the temperature inside the chamber increased as the deposition time increased. To alleviate this issue, there was a few minute delay in between different layer depositions to allow for the chamber to cool down and for the pumps to remove the airborne deposition material.

4.1.2. Device Fabrication

Sample Preparation

The substrates were chosen to be 4" diameter, $500 \pm 25 \mu\text{m}$ thickness, single side polished, n-type $\{111\}$ test quality silicon wafers.

Before starting the initial depositions, the silicon wafers were dipped for 15 seconds in dilute HF to remove the native silicon dioxide from the silicon wafer's surface. Since the native oxide grows back within a relatively short amount of time (around a day), this was done immediately before the deposition [78]. After rinsing the wafer with DI water, it was baked at 90°C for three minutes to remove any water absorbed in the crystal lattice [79]. Following this, the wafer was placed on the chuck and then fixed using three clips. Then the sample was placed inside the e-beam PVD (Figure 4.4) which was already vented. After that, the e-beam PVD was pumped down to a vacuum pressure less than 2.5×10^{-5} Torr. During these steps, care was taken so that the wafer was kept as clean as possible and that there were no opportunities for contamination.

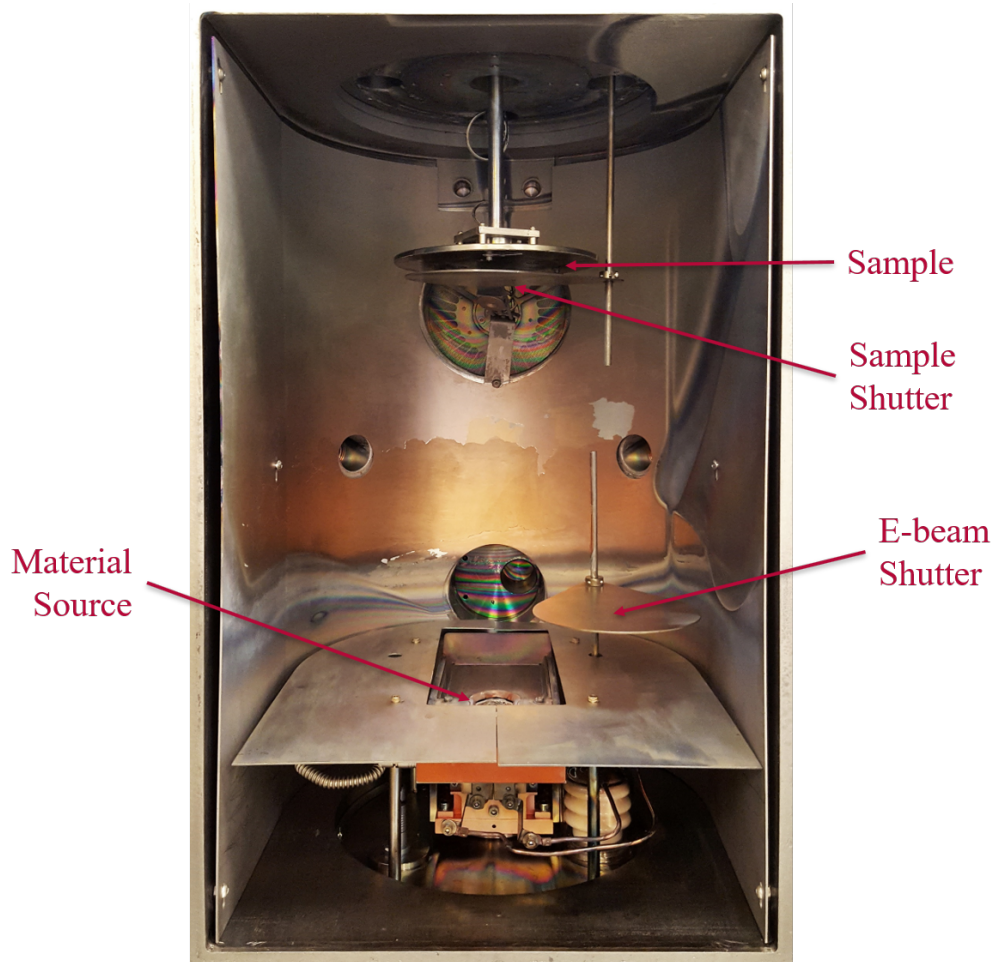


Figure 4.4: The PVD fabrication chamber used in the MiNDS facility [55]. The important machine components are labeled.

Device Fabrication

The fabrications took place over the period of several months. The first round of depositions were used to determine the optical properties of the deposited Cu and TiO₂. The first sample had ten nm of Cu deposited on a blank Si wafer, and the second sample had five nm of TiO₂ deposited on another blank Si wafer. In the next round, a Cu/TiO₂ HMM was fabricated. It had four periods of 15 nm each, for a total nominal thickness of 60 nm. This was followed by the OAD deposited Cu, where one micron of Cu was deposited at $\alpha = 70^\circ$. Then, more HMMs were made in the next round of fabrication in order to demonstrate the EMA technique for spectroscopic ellipsometry. In this round, additional samples were made with a 15 nm period, and devices with a 20 nm period were fabricated. Finally, HMMs made from Al/TiO₂ were fabricated with three periods of 50 nm thickness for a total thickness of 150 nm.

4.2. Characterization

4.2.1. Spectroscopic Ellipsometry

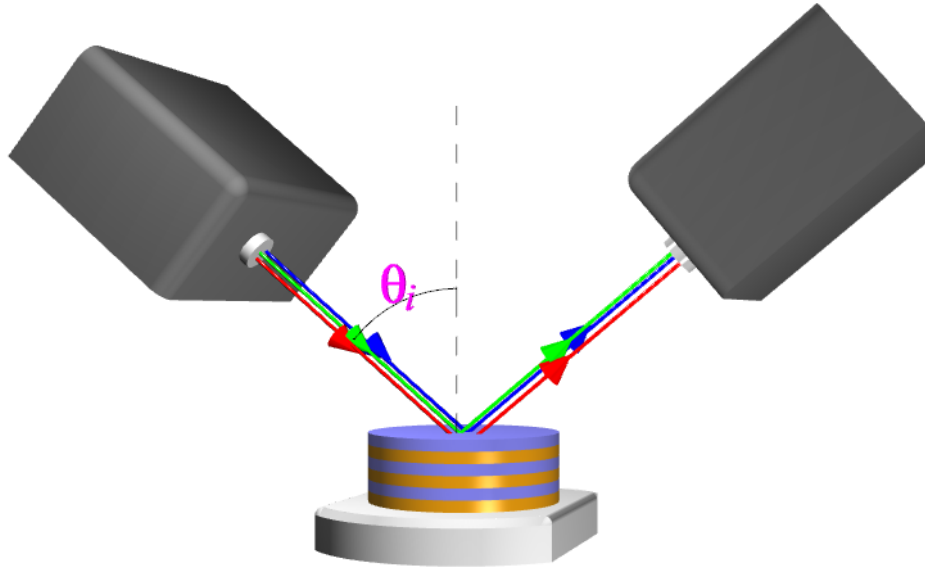


Figure 4.5: Spectroscopic ellipsometry configuration used in this work. Three different values of θ_i were used: 65° , 70° , and 75° . The visible spectrum of light was measured from 380 to 890 nm.

Spectroscopic ellipsometric measurements have previously been used to characterize HMMs [20]. Reflection mode spectroscopic ellipsometry sends a polarized beam of light and then measures the change in polarization of the reflected light (Figure 4.5). This change in polarization state is defined by the relation

$$\tan \Psi \cdot e^{i\Delta} = \frac{r_p}{r_s} = \rho, \quad (4.1)$$

where r_s is the complex amplitude reflectance for s polarization (in-plane), r_p is the complex amplitude reflectance for p polarization (out-of-plane), Ψ is the magnitude of the ellipsometric

reflectivity ratio, and Δ is the ellipsometric phase term [80]. All of the values are dependent on the incident angle of the polarized light θ . By using multiple wavelengths, spectroscopic ellipsometry is able to provide unique answers for material parameters, have an improved sensitivity to material properties, and give data at desired wavelengths compared to monochromatic measurements. An α -SE Ellipsometer from J.A. Wollam (Figure. 4.6) running CompleteEase software was used for measurements of the fabricated device. The anisotropic Mueller-matrix (MM) was used to specify the interaction of light with the HMM sample. Three measurements were taken at 65° , 70° , and 75° , respectively. Ellipsometry measurements are typically taken near the Brewster angle, but this is less important with ellipsometers that include compensators such as the α -SE. As the complexity of the sample increases, more incident angles of measurement should be used to produce good data. A rotating compensator was also used to manipulate the polarization state to improve results further. The compensator was spun continuously to adjust the retardance and allow the measured SE data to be calculated from many simultaneous polarizations; this was handled by the CompleteEASE software and did not have to be done by the user. A silicon substrate was used to eliminate back-reflection from the sample.

By themselves, Ψ and Δ are not informative, and so various equations and algorithms must be used to model the interaction of light with the sample, enabling the model parameters to be extracted. The shape of the oscillations of Ψ and Δ depends on the film index of refraction, allowing for the complex index of refraction to be extracted.

If the measurement system and sample are ideal, the incoming and received light would be fully polarized. However, in real-world conditions, some of the light becomes depolarized. This depolarization was also measured to help quantify the effects of the thin films [81].

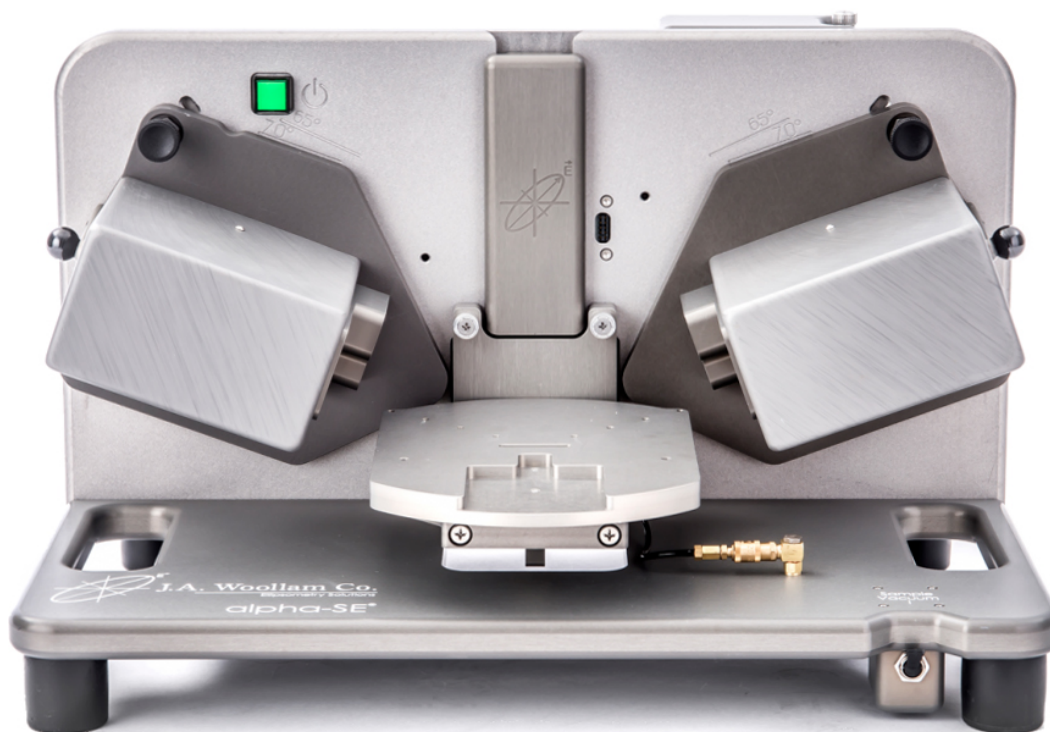


Figure 4.6: The α -SE Ellipsometer used for characterization of HMM samples [82].

4.2.2. TIR Ellipsometry

Another technique known as TIR ellipsometry, previously mentioned in Chapter 1, uses a prism to couple light into the sample after it undergoes total internal reflection [23], which improves the characterization of thin semitransparent films [24] and has previously been used to successfully characterize HMMs [20]. In TIR ellipsometry, the prism, optical matching gel, and fused silica substrate are represented as a single layer in the ellipsometric model. This more complicated model, in addition to the presence of back reflections, means that the TIR ellipsometric modeling procedure is inherently more complex than the procedure used in standard spectroscopic ellipsometry. Additionally, the prism makes it difficult to do measurements in an in-line process as is widely used to characterize thin films in industrial settings [83].

Zhang et al. used an iterative modeling process based on transfer-matrix-method (TMM) cal-

culations for the TIR ellipsometric process. A homogenous, uniaxial model was used with the imaginary part of the in-plane direction modeled as with a B-spline curve, and the imaginary part of the out of plane direction modeled with a two-oscillator model $\Im\{\epsilon_{\perp}\} = \Im\{\epsilon_{Lorentz}\} + \Im\{\epsilon_{Tauc-Lorentz}\}$. The real part of both permittivities was determined through the Kramers-Kronig rule. In the first stage of an iteration, the B-spline and oscillator parameters were set. Next, Ψ and Δ values were computed using TMM based on the values from the first stage. Finally, a regression analysis was used to compare the Ψ and Δ values and obtain the MSE. The process was iterated until a minimized MSE was obtained [20].

4.2.3. Our Spectroscopic Ellipsometry Technique

The in-plane direction was represented with a B-spline curve, whereas the out-of-plane direction was modeled using the Maxwell-Garnett EMA model. The EMA model in the CompleteEASE software is normally used to represent mixed-constituent layers caused by inter-layer roughness, surface roughness, and poly-crystalline materials [84]. The initial values of the EMA model were set to be the nominal fill factors with a depolarization of 1. The expected deposition values were used for the initial layer thicknesses. Additionally, angle offset was taken into account in the final model.

Initially, surface roughness was modeled; however, the MSE was minimized when the surface roughness was close to zero. Most likely, the software is accounting for the physical surface roughness in the EMA layer and angle offset. When the physical roughness was measured and used as a seed value, the extracted permittivity values did not change, demonstrating that successfully extracting the permittivity tensor does not depend on the software accounting for surface roughness. In order to correctly model the measured surface roughness, a dielectric layer with a thickness

of zero was added on the model. This caused the software to model the roughness in the top dielectric layer instead of in the effective material. The final process is shown as a flowchart in Figure. 4.7.

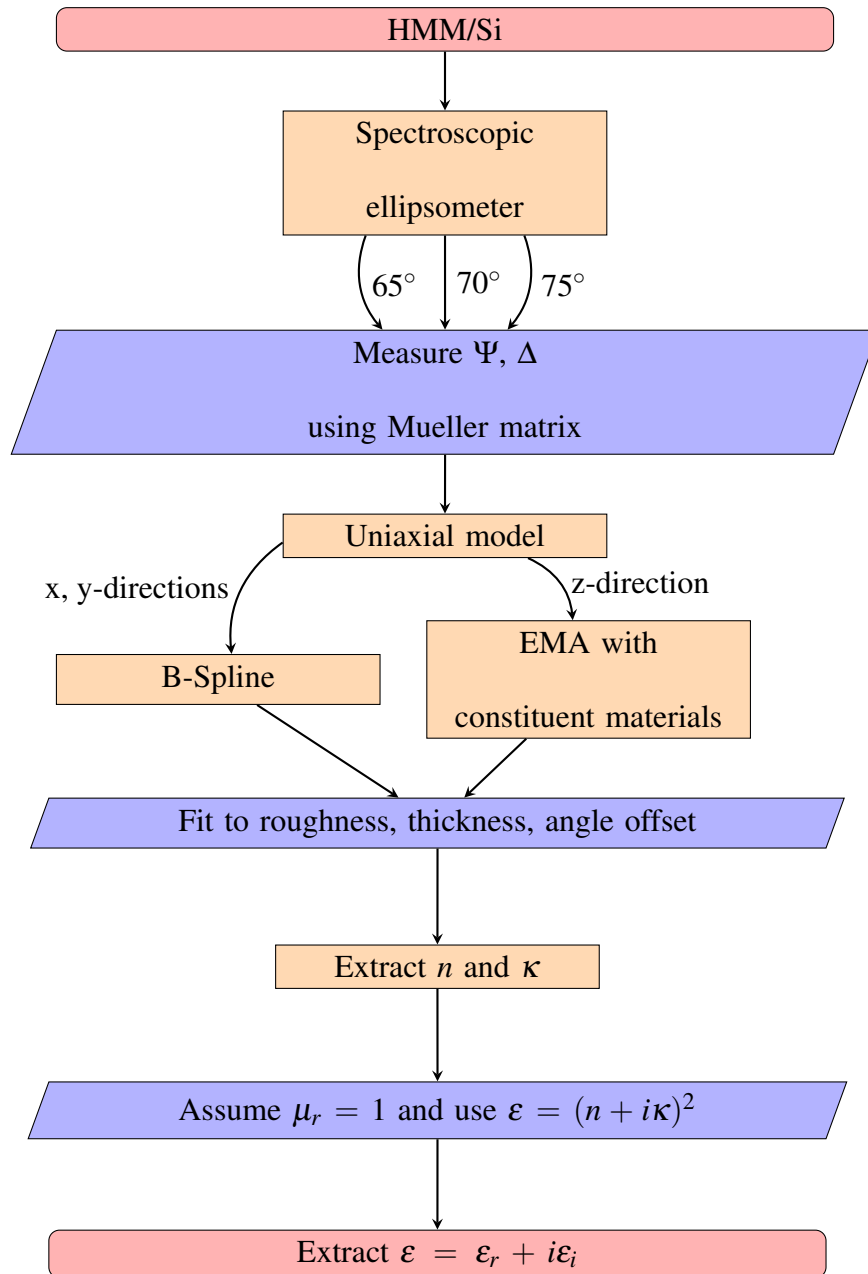


Figure 4.7: The spectroscopic ellipsometric process developed in this work for extracting the permittivity of HMMs.

5. DISCUSSION OF RESULTS

5.1. Summary

The results of all of the fabricated devices are shown in this chapter. The measured optical constants of as-deposited materials are shown in Figures 5.1 and 5.2, and the first HMM results are shown in Figures 5.5 and 5.6. Most importantly, the comparison of the extracted permittivities with the predictions provided by the initial EMT designs is shown in Figures 5.7. and 5.11. Additionally, We expected to observe a close correspondence between the calculated and measured values. In all cases, the dashed lines show the expected results based on the EMT calculations. The agreement obtained between all of the permittivities and their EMT-calculated values is satisfactory, since the procedure was able to accurately represent the out-of-plane permittivities in all cases where the samples were not contaminated. The type-II hyperbolic dispersion can be seen from these graphs, with a negative permittivity in the in-plane direction and a positive permittivity in the out-of-plane direction.

5.2. Material Constants

Ellipsometric measurements showed good agreement between the expected and obtained thicknesses for both TiO₂ and Cu. The titanium dioxide was modeled using the Cauchy equation as

$$n = 1.750 + \frac{0.04135}{\lambda^2} + \frac{0.00796}{\lambda^4}. \quad (5.1)$$

This had an MSE of 1.794. Figure 5.1 shows the modeled index of refraction. The thin film copper was modeled using a B-Spline curve. Figure 5.2 shows the measured thin-film values of the deposited copper which resulted in an MSE of 1.246.

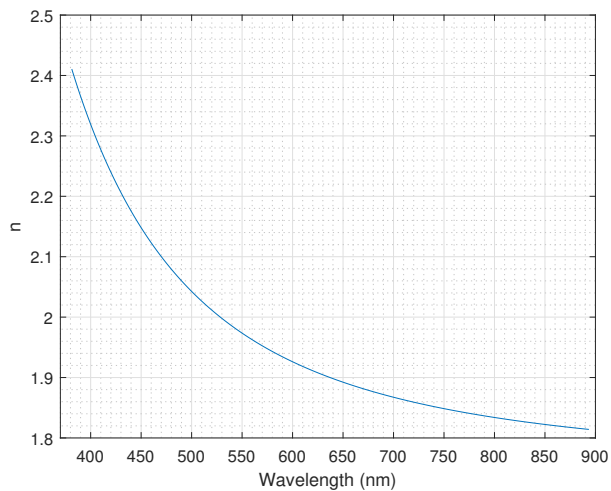


Figure 5.1: The index of refraction of the deposited TiO_2 determined by spectroscopic ellipsometry.

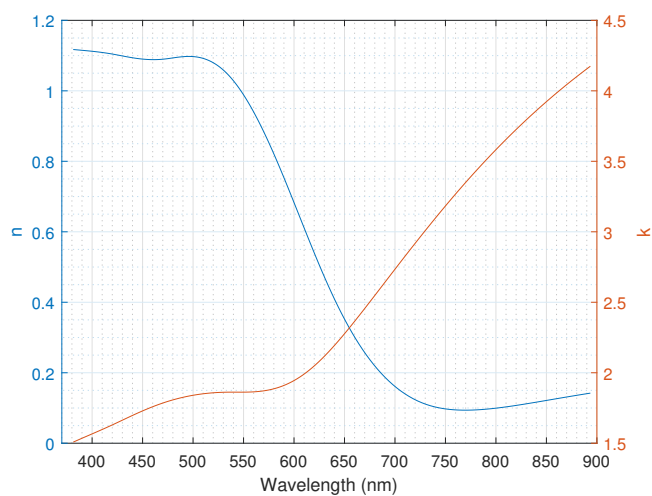


Figure 5.2: The optical constants of the deposited Cu determined by spectroscopic ellipsometry.

5.3. MSE Values

Figure 5.3 shows the model-fit Ψ and Δ compared to the measured values. It can be observed that the model is in very good agreement with the measurements, which promises low MSE values.

The MSE is defined as

$$MSE = \sqrt{\frac{1}{3n - m} \sum_{i=1}^n [(N_{meas,i} - N_{model,i})^2 + (C_{meas,i} - C_{model,i})^2 + (S_{meas,i} - S_{model,i})^2]} \times 1000, \quad (5.2)$$

where n is the number of wavelengths, m is the number of free parameters, and

$$N = \cos(2\Psi), \quad (5.3a)$$

$$C = \sin(2\Psi) \cos(\Delta), \quad (5.3b)$$

$$S = \sin(2\Psi) \sin(\Delta). \quad (5.3c)$$

Zhang et al. reported a best MSE of 11.72 [20], showing an improvement over current methods.

Several measurements were also made at different locations on each HMM sample to produce an estimate of the repeatability and reproducibility of the procedure. Remarkably, the MSE value obtained for each sample is achieved to be lower than 1.00. The MSE values for the ellipsometric modeling are shown in Table 5.1. Table 5.2 lists the best MSE values reported elsewhere for HMMs or plasmonic structures. The significance of the procedure described in Section 4.2.3 may now be more apparent.

Table 5.1: MSE Values for SE procedure described here.

HMM Structure	Period	Fill Factor	MSE
Cu/TiO ₂	15 nm	67%	0.72 ± 0.09
Cu/TiO ₂	20 nm	67%	0.63 ± 0.12
Al/TiO ₂	50 nm	90%	0.69 ± 0.10

Table 5.2: MSE Values reported elsewhere.

Structure	MSE	Ref.	Year
TiN	2-3	[85]	2019
Ag/Ta ₂ O ₅	24.96	[20]	2018
Ag/Ta ₂ O ₅	19.82	[20]	2018
Ag/Ta ₂ O ₅	11.72	[20]	2018
Ag/PVP	4.6	[17]	2017
Ag/PVP/PMMA	7.21	[17]	2017

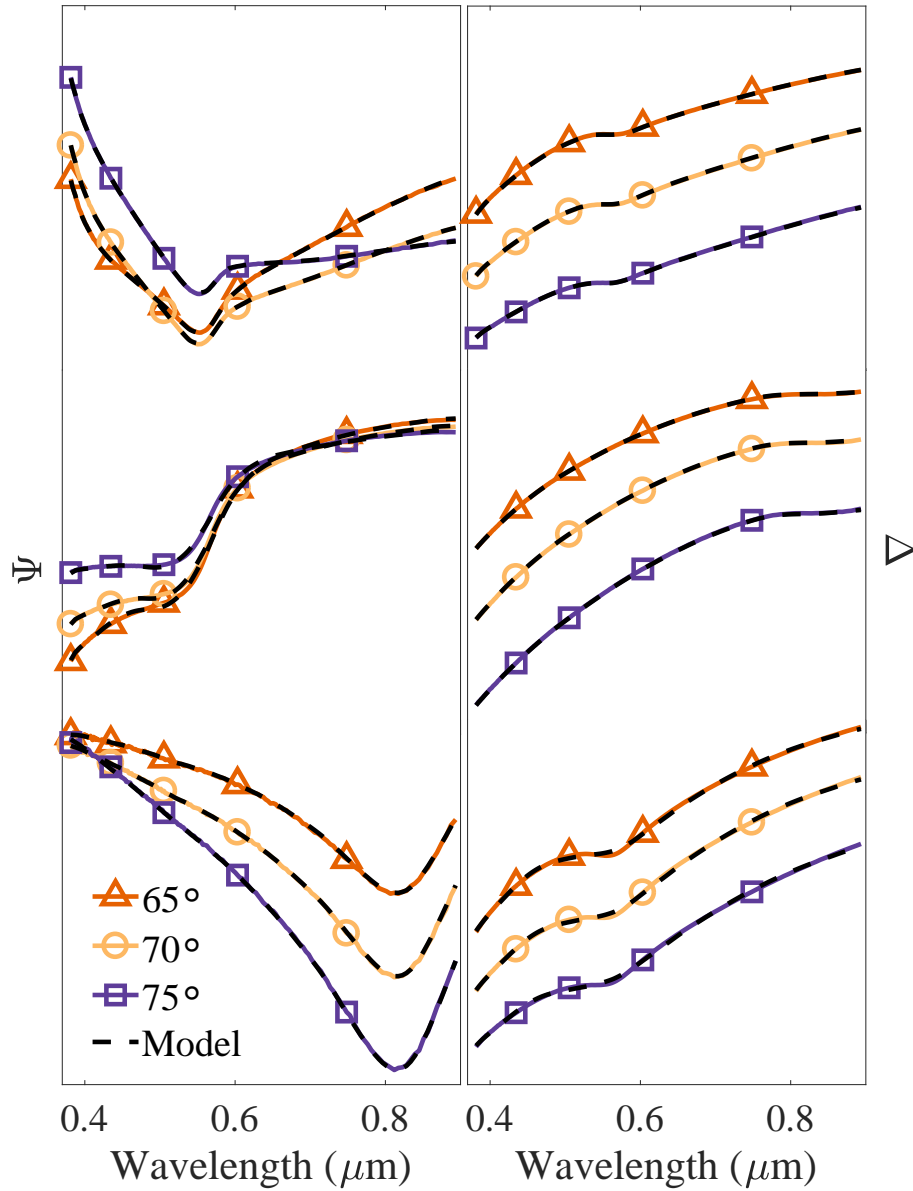


Figure 5.3: The Ψ and Δ model compared to the measured values. Included are results for both a Al/TiO_2 device (bottom three lines) and two Cu/TiO_2 devices (top six lines).

5.4. Surface Roughness

The surface roughnesses for both Cu/TiO₂ and Al/TiO₂ HMM samples were measured using the AFM. The results are shown in Figure 5.4 and Table 5.3.

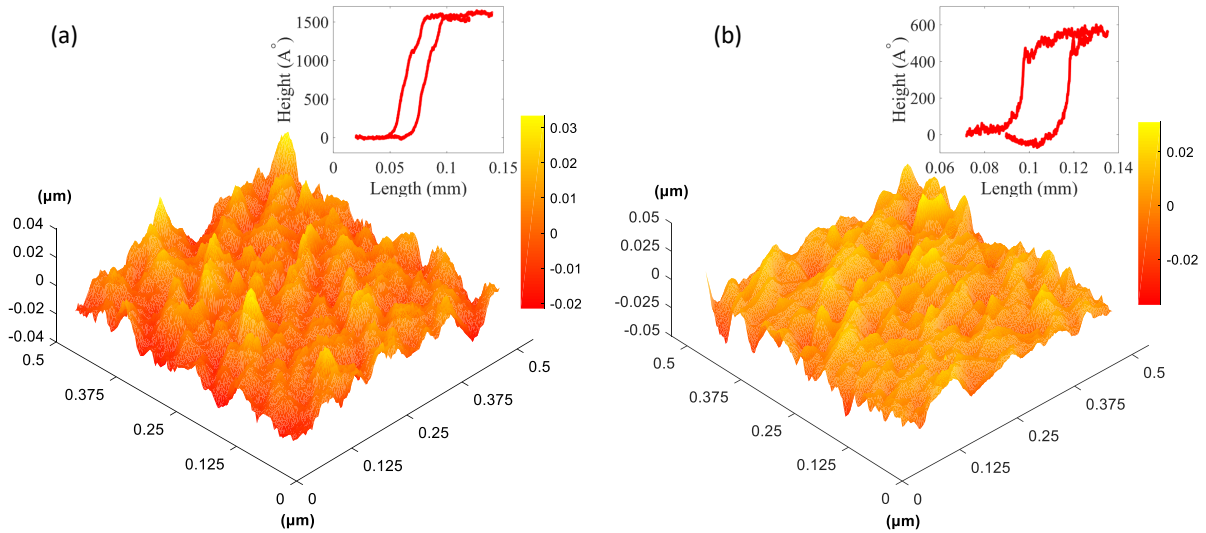


Figure 5.4: AFM measurements of surface roughness for the Al/TiO₂ sample (left) and the 15 nm period Cu/TiO₂ sample (right). The insets show profilometer data used to determine the total deposition thickness.

Table 5.3: Surface roughness as measured by AFM

Structure	Period	# of Periods	S_a	S_q
Cu/TiO ₂	15 nm	4	6.01 nm	7.59 nm
Cu/TiO ₂	20 nm	1	3.3 nm	4.1 nm
Al/TiO ₂	50 nm	3	5.92 nm	7.5 nm

5.5. Cu/TiO₂ HMM

5.5.1. EMA Model Spectroscopic Ellipsometry

The measured index of refraction of the first fabricated 15 nm Cu/TiO₂ multilayer HMM compared to the expected values is shown in Figure 5.5. The EMT calculation was based on the values measured with spectroscopic ellipsometry. Overall, there is good agreement between the two plots. The difference between the different values can be explained by differences in deposited materials such as layer thickness, roughness, strain, and electrical permittivities.

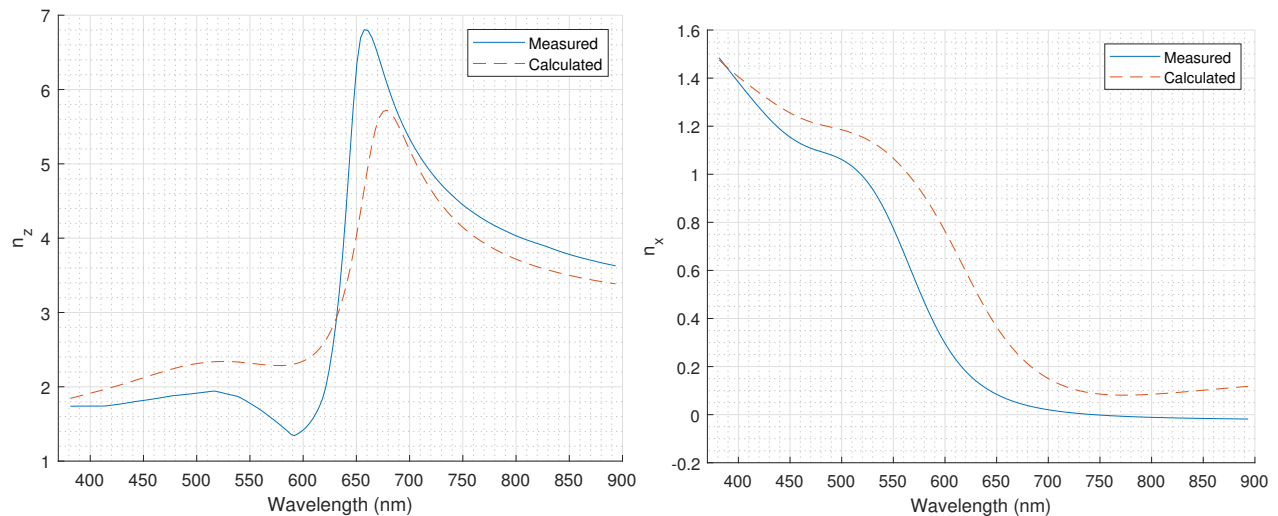


Figure 5.5: The expected index of refraction based on EMT with in-house measured permittivity values compared to the fabricated device as measured by spectroscopic ellipsometry.

Figure 5.6 shows the measured permittivities compared to the EMT calculations. Above a wavelength of around 633 nm, the device acts hyperbolic, having a negative permittivity in the x direction, and a positive permittivity in the z direction. The negative imaginary permittivity in the x and y directions is nonphysical and most likely due to a fitting error in the ellipsometric modeling, although metamaterials with negative imaginary parts of permittivity have been discussed. [86, 87]

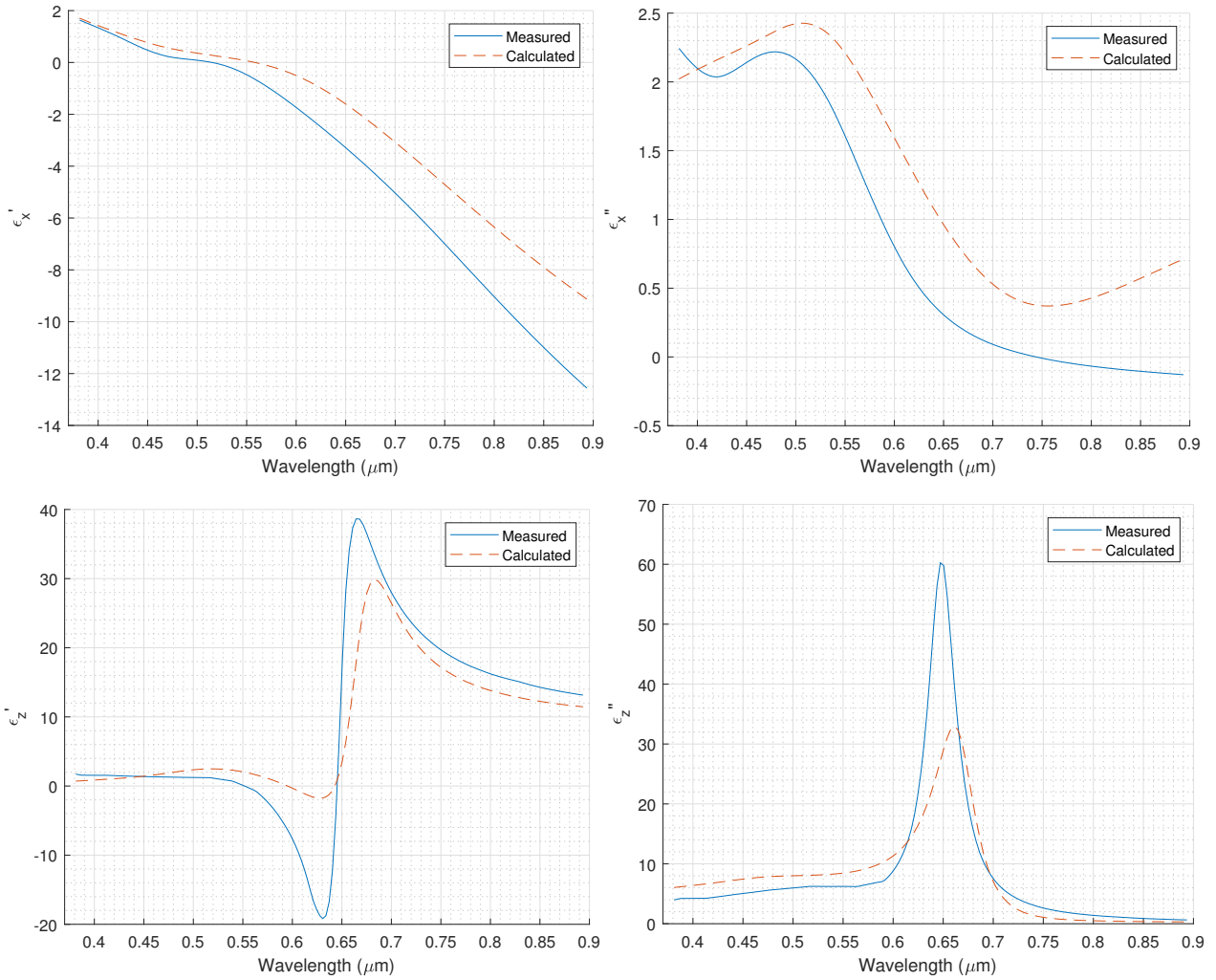


Figure 5.6: The permittivities based on EMT with in-house measured permittivity values compared to the fabricated device as measured by spectroscopic ellipsometry.

Additional Devices

The results for the 15 nm and 20 nm period Cu/TiO₂ devices are shown in Figure. 5.7. It should be noted that there is no longer a negative imaginary permittivity as was observed in the previous sample. Overall, there is good agreement between the EMT predicted values, the 15 nm period device, and the 20 nm period device. The small differences in permittivity are explainable by a difference in fill factors due to fabrication errors.

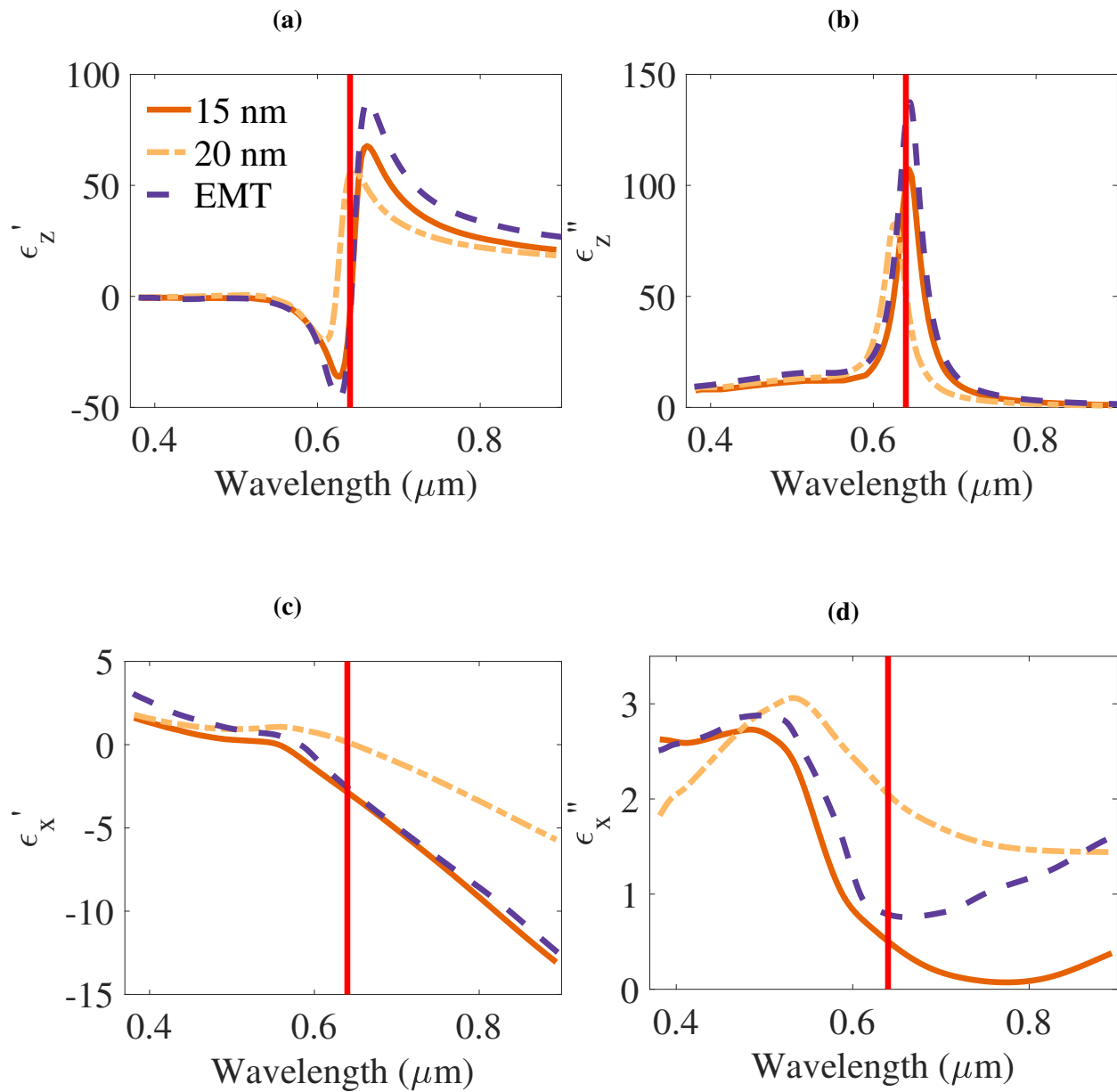


Figure 5.7: Results from the Cu/TiO₂ multilayers. Above the red line, the device acts hyperbolic. Two different periods were used: 15 nm and 20 nm. The EMT calculated permittivities (dotted lines) are compared to the fabricated values: 5.7(a) The real part of the out-of-plane permittivity; 5.7(b) The imaginary part of the out-of-plane permittivity; 5.7(c) The real part of the in-plane permittivity; 5.7(d) The imaginary part of the in-plane permittivity

5.5.2. TIR Ellipsometry

For our TIR ellipsometric measurements, a fused silica prism was placed in optical contact with the silica substrate through the use of index matching gel, which provides optical matching over the entire visible spectrum. Unfortunately, accurate permittivities were unable to be extracted using TIR ellipsometry. The z-direction permittivities had a smaller resonant response than what was predicted through EMT. The x and y directions showed a response more consistent with dielectric than with a metal, with a positive real part of permittivity. These results are shown in Figures 5.8 and 5.9.

Our conclusions are that the process involving the prism, gel, fused silica substrate as well as the iterative modeling process using transfer matrix method calculations is unnecessarily complex. While this procedure can work in a research setting, it would be difficult to implement in an industrial process, meaning that a simpler procedure should be developed and tested.

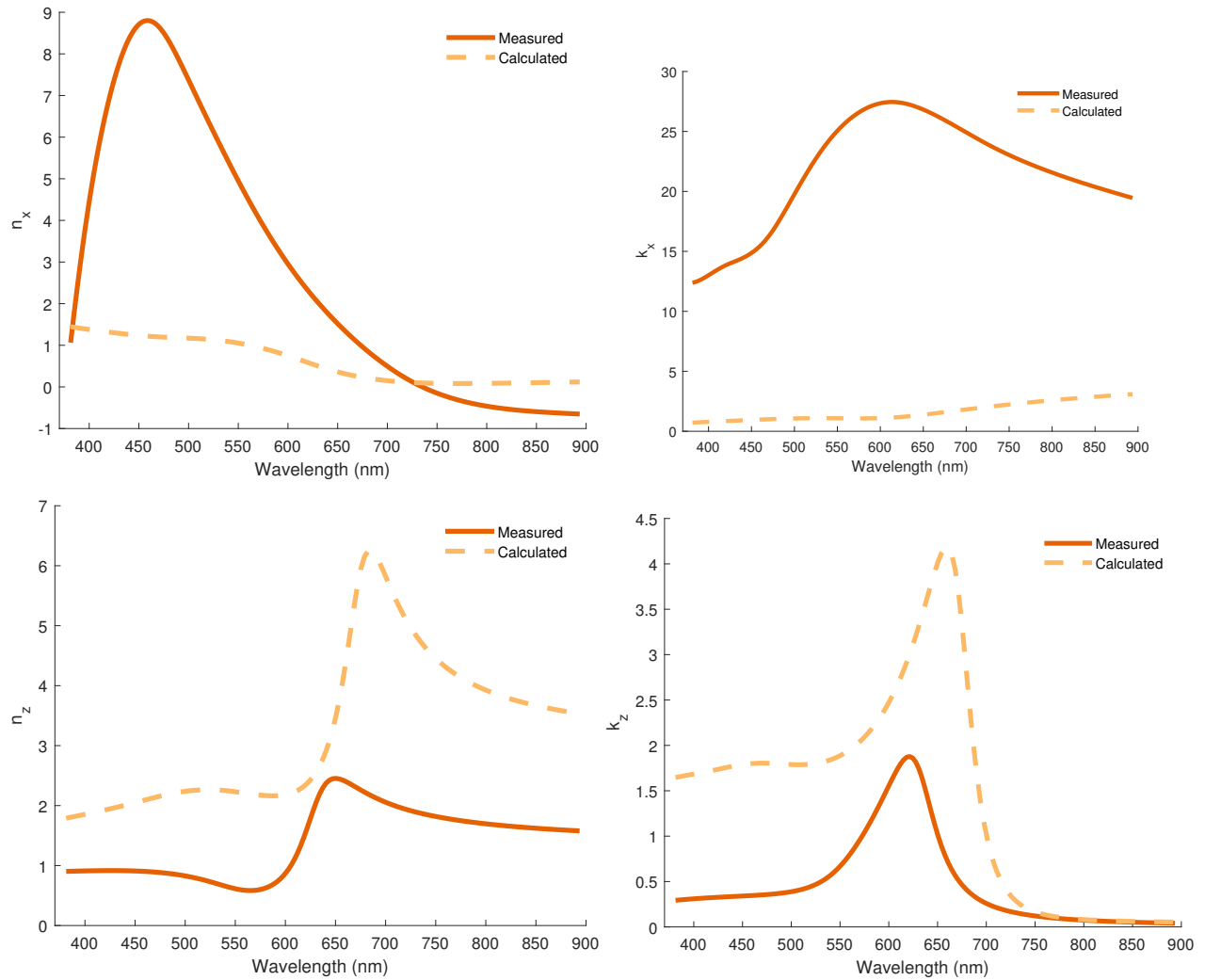


Figure 5.8: The indices of refraction based on EMT with in-house measured values compared to the fabricated device as measured by TIR ellipsometry.

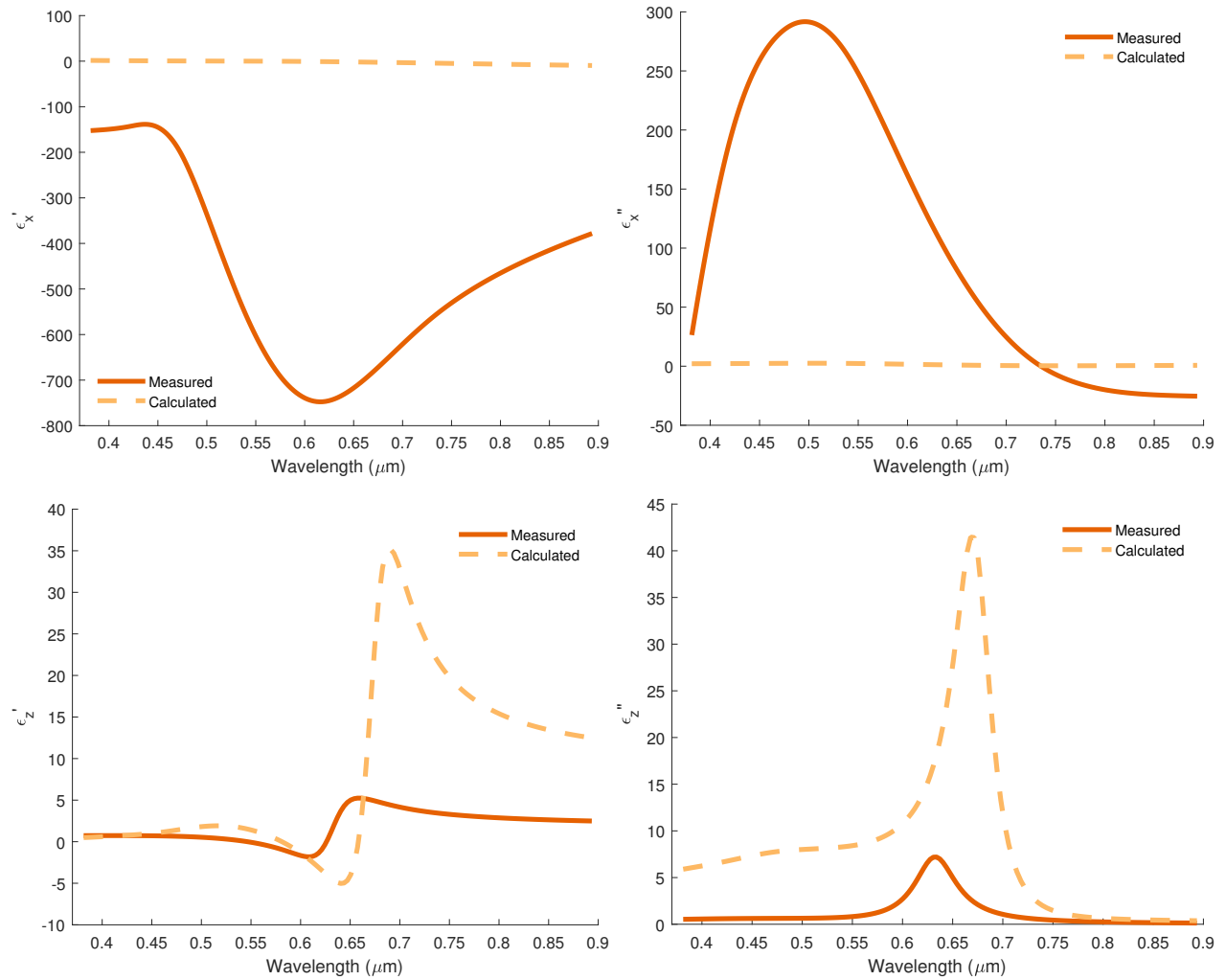


Figure 5.9: The permittivities based on EMT with in-house measured permittivity values compared to the fabricated device as measured by TIR ellipsometry.

5.6. Cu/Air HMM

The device simulated in Section 3.4 was fabricated, with a deposition thickness of one micron. Unfortunately, the measured optical constants of this material do not match their expected values. Moreover, they are most likely physically impossible since they show a negative imaginary part of electric permittivity [88] since the HMM would be adding energy to the system in violation of the Second Law of Thermodynamics [89]. SEM images of the sample were obtained to try and understand the device structure. However, the SEM in the MiNDS facility did not have a high enough magnification to resolve the features on the sample.

It is believed that the issues with these ellipsometric measurements are due to sample contamination, as the samples are visibly dirty. During fabrication, the sample shutter is not able to be used with the OAD deposition substrate holder, increasing the contamination that occurs during the e-beam ramping steps. These issues could be solved through optimization of the Cu deposition recipe or modification of the sample shutter so that it is able to be used during OAD depositions.

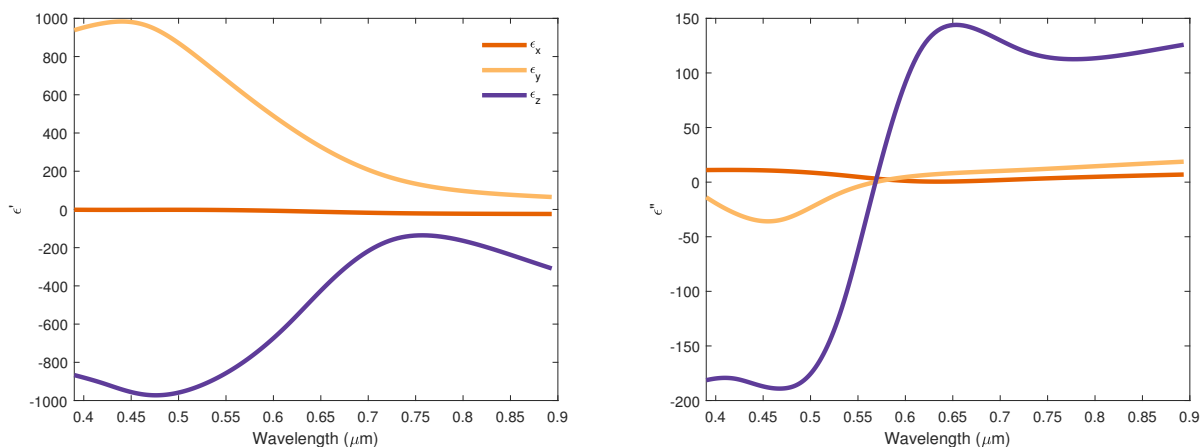


Figure 5.10: The measured of refraction for the Cu/Air HMM.

5.7. Al/TiO₂ HMM

As a part of demonstrating our technique for spectroscopic ellipsometry, HMMs consisting of Al and TiO₂ multilayers were also measured. The permittivity results compared to the EMT calculations are shown in Figures 5.7 and 3.5. In Figures 5.7(a) and 5.11(a), the real part of the out-of-plane permittivity is shown, in Figures 5.7(b) and 5.11(b) the imaginary part of the out-of-plane permittivity is shown, Figures 5.7(c) and 5.11(c) show the real part of the in-plane permittivity, and Figures 5.7(d) and 5.11(d) show the imaginary part of the in-plane permittivity. In all cases, the dashed line shows the expected results based on the EMT calculations.

By using an EMA ellipsometric model, accurate permittivities were able to be extracted. The HMMs were modeled as a uniaxial, homogenous material. The in-plane direction was represented with a B-spline curve whereas the out-of-plane direction was modeled using the Maxwell-Garnett EMA model. The EMA model in the CompleteEASE software is normally used to represent mixed-constituent layers caused by inter-layer roughness, surface roughness, and poly-crystalline materials [84]. The initial values of the EMA model were set to be the nominal fill factors with a depolarization of 1. The expected deposition values were used for the initial layer thicknesses. Surface roughness and angle offset were taken into account in the final model.

Excellent agreement is obtained between all of the permittivities and their EMT-calculated values. The ellipsometric EMA model was able to accurately represent the out-of-plane permittivities in all cases.

The type-II hyperbolic dispersion can be seen from these graphs, with a negative permittivity in the in-plane direction, and a positive permittivity in the out-of-plane direction. As the wavelength decreases, the material's real in-plane permittivity increases and real out-of-plane permittivity decreases, and it eventually loses its hyperbolicity at wavelengths less than the ENZ line.

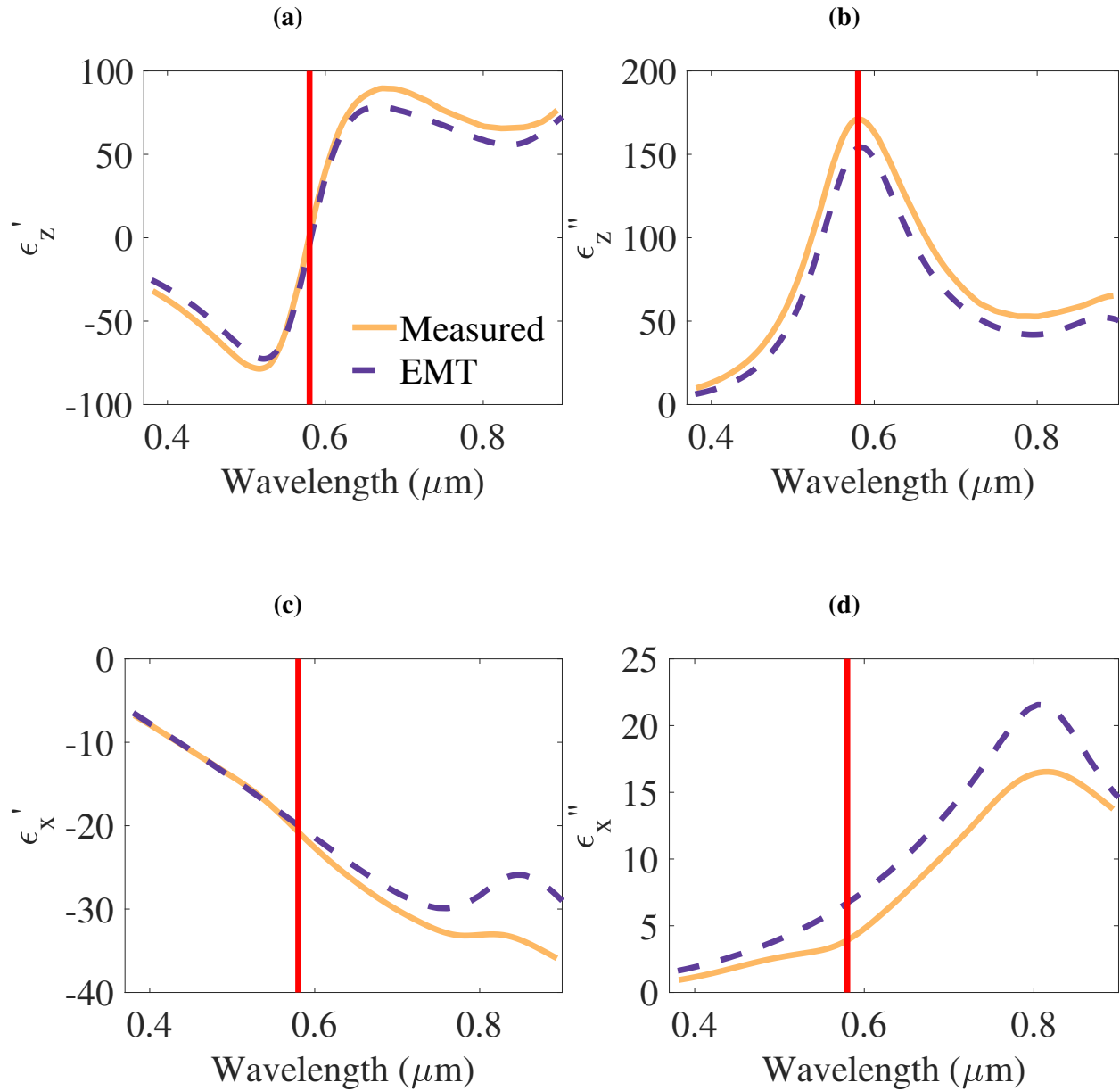


Figure 5.11: Results from the Al/TiO₂ multilayers. Above the red line, the device acts hyperbolic. The period for this device was 50 nm. The EMT calculated permittivities (dotted lines) are compared to the fabricated values (solid line).

6. CONCLUSION

The design, fabrication, and measurement of several hyperbolic metamaterials fabricated from multilayers of both Cu/TiO₂ and Al/TiO₂ with ENZ regions around the He-Ne wavelength was shown. The HMMs demonstrated extremely anisotropic behavior above the region around 633 nm, acting as metals in the x and y directions and as dielectrics in the z direction. When characterized by spectroscopic ellipsometry, the devices showed good agreement with theory. Additionally, the design of an HMM based on Cu nanowires and the design of a biaxial HMM based on Cu and OAD-deposited TiO₂ were presented, although neither of them were successfully fabricated.

Most importantly, a procedure for characterization of HMMs was described and demonstrated, which accurately retrieves the complex permittivity tensor in a time efficient, cost effective, and low-MSE approach. By using an EMA model for the out-of-plane permittivity, accurate results have been achieved, eliminating the need for more complicated measurement techniques such as TIR ellipsometry. Since the procedure was only dependent on software, it can be easily and widely adopted. Furthermore, the procedure would have a potential application in in-line CMOS processing due to its versatility and independence from additional optical elements or equipment, which in turn expands its utility. Three samples of varying fill factors and materials were fabricated, and all were successfully characterized using the procedure. All of the MSE values obtained were all below the desired value of 1.00, while at the same time meaningful and reasonable permittivities were extracted from HMMs.

6.1. Future Work

There are several steps that could be taken to further complete this work. First, the exact theoretical behavior of the HMMs should be determined using TMM simulations. This will provide a better idea of how the device should behave and would help explain some of the differences between EMT calculations and measured behavior. Next, the fabrication and characterization techniques developed here should be applied to produce one of the many HMM applications. A good application would be using HMMs to couple light into waveguides. In order to successfully couple light, there must be matching between the k -vectors of the free space and waveguide. Since HMMs are indefinite and can support unbounded k -states, it would be possible to use an HMM for k -matching, enabling HMM waveguide coupling. A significant amount of research in the MiNDs facility is in the field of silicon photonics and waveguide coupling, making this a good fit for Rose-Hulman. Further fabrication and testing of biaxial metamaterials should also be conducted to obtain a HMM where the behavior in all three Cartesian coordinates is separately engineered. Additionally, it should be possible to successfully fabricate a Cu/Air HMM, including capturing pictures of the nanopillars with a more powerful SEM. This could be done by optimizing the current fabrication recipe and equipment or by outsourcing fabrication to another cleanroom facility. Finally, our fabrication and characterization method can be extended to other wavelengths of interest such as $1.55 \mu\text{m}$ for fiber optics telecommunications.

LIST OF REFERENCES

- [1] Richard A Shelby, David R Smith, and Seldon Schultz. “Experimental verification of a negative index of refraction”. In: *science* 292.5514 (2001), pp. 77–79.
- [2] Jessica Bénédicte, Emmanuel Centeno, and Antoine Moreau. “Lens equation for flat lenses made with hyperbolic metamaterials”. In: *Optics letters* 37.22 (2012), pp. 4786–4788.
- [3] Christophe Caloz and Tatsuo Itoh. *Electromagnetic Metamaterials*. Wiley-IEEE Press, 2006.
- [4] Lorenzo Ferrari et al. “Hyperbolic Metamaterials and Their Applications”. In: *Progress in Quantum Electronics* (2014).
- [5] Hossein Alisafae and Michael A Fiddy. “Nanoantennas for nanowire photovoltaics”. In: *Applied Physics Letters* 105.11 (2014), p. 113107.
- [6] Wei Ting Chen et al. “A broadband achromatic polarization-insensitive metalens consisting of anisotropic nanostructures”. In: *Nature communications* 10.1 (2019), p. 355.
- [7] Dylan Lu and Zhaowei Liu. “Hyperlenses and metalenses for far-field super-resolution imaging”. In: *Nature communications* 3 (2012), p. 1205.
- [8] Tengfei Li and Jacob B Khurgin. “Hyperbolic metamaterials: beyond the effective medium theory”. In: *Optica* 3.12 (2016), pp. 1388–1396.
- [9] T Galfsky et al. “Active hyperbolic metamaterials: enhanced spontaneous emission and light extraction”. In: *Optica* 2.1 (2015), pp. 62–65.
- [10] Patrice Genevet et al. “Recent advances in planar optics: from plasmonic to dielectric metasurfaces”. In: *Optica* 4.1 (2017), pp. 139–152.
- [11] Kezhang Shi, Fanglin Bao, and Sailing He. “Enhanced Near-Field Thermal Radiation Based on Multilayer Graphene-hBN Heterostructures”. In: *ACS Photonics* 4.4 (2017), pp. 971–978. DOI: 10.1021/acsp Photonics.7b00037. eprint: <https://doi.org/10.1021/acsp Photonics.7b00037>. URL: <https://doi.org/10.1021/acsp Photonics.7b00037>.
- [12] Alexander Poddubny et al. “Hyperbolic metamaterials”. In: *Nature Photonics* 7 (2013), pp. 948–957.
- [13] Yongmin Liu, Guy Bartal, and Xiang Zhang. “All-angle negative refraction and imaging in a bulk medium made of metallic nanowires in the visible region”. In: *Optics Express* 16 (2008), pp. 15439–15448.
- [14] Elena Mikheeva et al. “Hyperbolic metamaterials based on metal-dielectric thin layers”. In: vol. 10691. 2018, pp. 10691–10691–9. DOI: 10.1117/12.2313216. URL: <https://doi.org/10.1117/12.2313216>.
- [15] F Peragut et al. “Hyperbolic metamaterials and surface plasmon polaritons”. In: *Optica* 4.11 (2017), pp. 1409–1415.

- [16] M. Born and E. Wolf. *Principles of Optics*. seventh. Cambridge University Press, 1959.
- [17] Miriam Carlberg et al. “Spectroscopic ellipsometry study of silver nanospheres and nanocubes in thin film layers”. In: *Opt. Mater. Express* 7.12 (2017), pp. 4241–4248. DOI: 10.1364/OME.7.004241. URL: <http://www.osapublishing.org/ome/abstract.cfm?URI=ome-7-12-4241>.
- [18] Principia Dardano et al. “Ellipsometric determination of permittivity in a negative index photonic crystal metamaterial”. In: *Light: Science & Applications* 1.12 (2012), e42.
- [19] Thomas WH Oates et al. “Oblique incidence ellipsometric characterization and the substrate dependence of visible frequency fishnet metamaterials”. In: *Optics express* 20.10 (2012), pp. 11166–11177.
- [20] Cheng Zhang et al. “Robust Extraction of Hyperbolic Metamaterial Permittivity Using Total Internal Reflection Ellipsometry”. In: *ACS Photonics* 5.6 (2018), pp. 2234–2242. DOI: 10.1021/acsp Photonics.8b00086. eprint: <https://doi.org/10.1021/acsp Photonics.8b00086>. URL: <https://doi.org/10.1021/acsp Photonics.8b00086>.
- [21] William A McGahan, Blaine Johs, and John A Woollam. “Techniques for ellipsometric measurement of the thickness and optical constants of thin absorbing films”. In: *Thin Solid Films* 234.1-2 (1993), pp. 443–446.
- [22] James N Hilfiker et al. “Survey of methods to characterize thin absorbing films with spectroscopic ellipsometry”. In: *Thin Solid Films* 516.22 (2008), pp. 7979–7989.
- [23] Michal Poksinski and Hans Arwin. “In situ monitoring of metal surfaces exposed to milk using total internal reflection ellipsometry”. In: *Sensors and Actuators B: Chemical* 94.3 (2003), pp. 247–252. ISSN: 0925-4005. DOI: [https://doi.org/10.1016/S0925-4005\(03\)00382-4](https://doi.org/10.1016/S0925-4005(03)00382-4). URL: <http://www.sciencedirect.com/science/article/pii/S0925400503003824>.
- [24] Hans Arwin, Michal Poksinski, and Knut Johansen. “Total internal reflection ellipsometry: principles and applications”. In: *Appl. Opt.* 43.15 (2004), pp. 3028–3036. DOI: 10.1364/AO.43.003028. URL: <http://ao.osa.org/abstract.cfm?URI=ao-43-15-3028>.
- [25] Thejaswi Tumkur et al. “Permittivity evaluation of multilayered hyperbolic metamaterials: Ellipsometry vs. Reflectometry”. In: *Journal of Applied Physics* 117 (2015), p. 103104. DOI: 10.1063/1.4914524.
- [26] Frank L. Pedrotti S.J., Leno M. Pedrotti, and Leno S. Pedrotti. *Introduction to Optics: Pearson New International Edition*. Pearson Education Limited, 2013.
- [27] J.R. Reitz, F.J. Milford, and R.W. Christy. *Foundations of Electromagnetic Theory*. Pearson/Addison-Wesley, 2009.
- [28] A. Yariv and P. Yeh. *Optical Waves in Crystals: Propagation and Control of Laser Radiation*. Wiley Series in Pure and Applied Optics. Wiley, 2002.
- [29] Grant R. Fowles. *Introduction to Modern Optics*. Second. Holt, Rinehart, and Winston, 1975.
- [30] Viktor G Veselago. “The electrodynamics of substances with simultaneously negative values of ϵ and μ ”. In: *Soviet Physics Uspekhi* 10.4 (1968), pp. 509–514.

- [31] B.E.A. Saleh and M.C. Teich. *Fundamentals of Photonics*. Wiley Series in Pure and Applied Optics. Wiley, 2007.
- [32] R.C. Buchanan and T. Park. *Materials Crystal Chemistry*. Taylor & Francis, 1997.
- [33] GE Jellison and FA Modine. “Two-modulator generalized ellipsometry: theory”. In: *Applied optics* 36.31 (1997), pp. 8190–8198.
- [34] GE Jellison Jr. “The calculation of thin film parameters from spectroscopic ellipsometry data”. In: *Thin Solid Films* 290 (1996), pp. 40–45.
- [35] GE Jellison Jr and JW McCamy. “Sample depolarization effects from thin films of ZnS on GaAs as measured by spectroscopic ellipsometry”. In: *Applied physics letters* 61.5 (1992), pp. 512–514.
- [36] R Joerger et al. “Influence of incoherent superposition of light on ellipsometric coefficients”. In: *Applied optics* 36.1 (1997), pp. 319–327.
- [37] Amnon Yariv and Pochi Yeh. *Optical Waves in Crystals*. Wiley Classics Library. John Wiley & Sons, Inc., 2003.
- [38] S. Song et al. “Biaxial hyperbolic metamaterials using anisotropic few-layer black phosphorus”. In: *Optics Express* 26 (5 2018).
- [39] I. A. Kolmychek et al. “Magneto-optical effects in hyperbolic metamaterials”. In: *Opt. Lett.* 43.16 (2018), pp. 3917–3920. DOI: 10.1364/OL.43.003917. URL: <http://ol.osa.org/abstract.cfm?URI=ol-43-16-3917>.
- [40] Andrew Joseph Hohne. “Development of polarizing spectral bandpass filter using dual sub-wavelength metallic gratings”. Montana State University-Bozeman, College of Engineering, 2017.
- [41] Andrew J Hohne et al. “Polarization-selective infrared bandpass filter based on a two-layer subwavelength metallic grating”. In: *Polarization Science and Remote Sensing VIII*. Vol. 10407. International Society for Optics and Photonics. 2017, 104070H.
- [42] Philippe Lalanne and Jean-Paul Hugonin. “High-order effective-medium theory of subwavelength gratings in classical mounting: application to volume holograms”. In: *J. Opt. Soc. Am. A* 15.7 (1998), pp. 1843–1851. DOI: 10.1364/JOSAA.15.001843. URL: <http://josaa.osa.org/abstract.cfm?URI=josaa-15-7-1843>.
- [43] Wenshan Cai et al. “Optical cloaking with metamaterials”. In: *Nature photonics* 1.4 (2007), p. 224.
- [44] Garnett JC Maxwell. “Colours in metal glasses and metal films”. In: *Philos. Trans. R. Soc. London, Sect. A* 3 (1904), pp. 385–420.
- [45] I. Richter et al. “Design considerations of form birefringent microstructures”. In: *Applied Optics* 34 (14 1995), pp. 2421–2429.
- [46] Enis Tuncer. “Structure–property relationship in dielectric mixtures: application of the spectral density theory”. In: *Journal of Physics D: Applied Physics* 38.2 (2005), p. 223.
- [47] P. B. Johnson and R. W. Christy. “Optical constants of the noble metals”. In: *Physical Review B* 6 (1972), pp. 4370–4379.

- [48] T. Siefke et al. “Materials pushing the application limits of wire grid polarizers further into the deep ultraviolet spectral range”. In: *Advanced Optical Materials* 4 (11 2016), pp. 1780–1786.
- [49] Prashant Shekhar, Jonathan Atkinson, and Zubin Jacob. “Hyperbolic metamaterials: fundamentals and applications”. In: *Nano convergence* 1.1 (2014), p. 14.
- [50] Kevin M McPeak et al. “Plasmonic films can easily be better: rules and recipes”. In: *ACS photonics* 2.3 (2015), pp. 326–333.
- [51] Tomoyoshi Motohiro and Yasunori Taga. “Thin film retardation plate by oblique deposition”. In: *Applied optics* 28.13 (1989), pp. 2466–2482.
- [52] L Holland. “The effect of vapor incidence on the structure of evaporated aluminum films”. In: *JOSA* 43.5 (1953), pp. 376–380.
- [53] DO Smith, MS Cohen, and Weiss. “Oblique-incidence anisotropy in evaporated Permalloy films”. In: *Journal of Applied Physics* 31.10 (1960), pp. 1755–1762.
- [54] MS Cohen. “Anisotropy in permalloy films evaporated at grazing incidence”. In: *Journal of Applied Physics* 32.3 (1961), S87–S88.
- [55] Ehsan Ordouie. “Design, Fabrication, and Characterization of a One-Dimensional Single Material Polarizing Photonic Crystal”. MA thesis. Rose-Hulman Institute of Technology, 2018.
- [56] Gorachand Ghosh. “Dispersion-equation coefficients for the refractive index and birefringence of calcite and quartz crystals”. In: *Optics communications* 163.1-3 (1999), pp. 95–102.
- [57] Viktor Elofsson et al. “Tilt of the columnar microstructure in off-normally deposited thin films using highly ionized vapor fluxes”. In: *Journal of Applied Physics* 113.17 (2013), p. 174906.
- [58] Liang Chen et al. “Engineering epitaxial-nanospiral metal films using dynamic oblique angle deposition”. In: *Crystal Growth & Design* 13.5 (2013), pp. 2075–2080.
- [59] Ehsan Ordouie, Hossein Alisafae, and Azad Siahmakoun. “Ultracompact polarizing beam splitter based on single-material birefringent photonic crystal”. In: *Opt. Lett.* 43.17 (2018), pp. 4288–4291. DOI: 10.1364/OL.43.004288. URL: <http://ol.osa.org/abstract.cfm?URI=ol-43-17-4288>.
- [60] Satoshi Ishii et al. “Sub-wavelength interference pattern from volume plasmon polaritons in a hyperbolic medium”. In: *Laser & Photonics Reviews* 7.2 (2013), pp. 265–271.
- [61] N. N. Greenwood. *Chemistry of the elements*. Oxford Boston: Butterworth-Heinemann, 1997.
- [62] H Tang et al. “Electrical and optical properties of TiO₂ anatase thin films”. In: *Journal of applied physics* 75.4 (1994), pp. 2042–2047.
- [63] M Landmann, E Rauls, and WG Schmidt. “The electronic structure and optical response of rutile, anatase and brookite TiO₂”. In: *Journal of physics: condensed matter* 24.19 (2012), p. 195503.

- [64] Charles McHenry. *The New Encyclopedia Britannica 3*. Chicago: Encyclopedia Britannica, 1992.
- [65] Cécile Delacour et al. “Efficient directional coupling between silicon and copper plasmonic nanoslot waveguides: toward metal- oxide- silicon nanophotonics”. In: *Nano letters* 10.8 (2010), pp. 2922–2926.
- [66] Sozo Yokogawa, Stanley P Burgos, and Harry A Atwater. “Plasmonic color filters for CMOS image sensor applications”. In: *Nano Letters* 12.8 (2012), pp. 4349–4354.
- [67] Mark W Knight et al. “Aluminum for plasmonics”. In: *ACS nano* 8.1 (2013), pp. 834–840.
- [68] Heung Yong Ha et al. “Properties of the TiO₂ membranes prepared by CVD of titanium tetraisopropoxide”. In: *Journal of membrane science* 111.1 (1996), pp. 81–92.
- [69] KK Saini et al. “Structural and optical properties of TiO₂ thin films derived by sol–gel dip coating process”. In: *Journal of non-crystalline solids* 353.24-25 (2007), pp. 2469–2473.
- [70] Jaan Aarik et al. “Effect of crystal structure on optical properties of TiO₂ films grown by atomic layer deposition”. In: *Thin Solid Films* 305.1-2 (1997), pp. 270–273.
- [71] S Yamamoto et al. “Preparation of epitaxial TiO₂ films by pulsed laser deposition technique”. In: *Thin Solid Films* 401.1-2 (2001), pp. 88–93.
- [72] Yanru Xie et al. “Epitaxial rutile TiO₂ film based on MgF₂ substrate for ultraviolet detector”. In: *Journal of Alloys and Compounds* 683 (2016), pp. 439–443.
- [73] MH Suhail, G Mohan Rao, and S Mohan. “DC Reactive Magnetron Sputtering of Titanium-Structural and Optical Characterization of TiO₂ Films”. In: *Journal of Applied Physics* 71.3 (1992), pp. 1421–1427.
- [74] Andy C van Popta et al. “Birefringence enhancement in annealed TiO₂ thin films”. In: *Journal of applied Physics* 102.1 (2007), p. 013517.
- [75] KS Sree Harsha. *Principles of vapor deposition of thin films*. Elsevier, 2005.
- [76] Kurt J. Lesker Company. *E-beam Evaporation of Titanium Dioxide (TiO₂)*. [Accessed: 2-June-2018]. URL: https://www.lesker.com/newweb/deposition_materials/depositionmaterials_evaporationmaterials_1.cfm?pgid=ti4b.
- [77] N Bundaleski et al. “Adsorption dynamics of water on the surface of TiO₂ (110)”. In: *Journal of Physics: Conference Series*. Vol. 257. 1. IOP Publishing, 2010, p. 012008.
- [78] Marin Alexe and Ulrich Gösele. *Wafer bonding: applications and technology*. Vol. 75. Springer Science & Business Media, 2013.
- [79] Sami Franssila. *Introduction to microfabrication*. John Wiley & Sons, 2010.
- [80] Hiroyuki Fujiwara. *Spectroscopic ellipsometry: principles and applications*. John Wiley & Sons, 2007.
- [81] Harland Tompkins and Eugene A Irene. *Handbook of ellipsometry*. William Andrew, 2005.
- [82] J.A. Woollam Co. *alpha-SE Ellipsometer*. [Accessed: 9-July-2018]. URL: <https://www.jawoollam.com/products/alpha-se-ellipsometer>.

- [83] Stefan Zollner. “Spectroscopic Ellipsometry for Inline Process Control in the Semiconductor Industry”. In: Springer Berlin Heidelberg, Mar. 2013, pp. 607–627. ISBN: 978-3-642-33955-4. DOI: 10.1007/978-3-642-33956-1_18.
- [84] Inc. J. A. Woollam Co. *CompleteEASE™ Data Analysis Manual*. English. Version Version 3.65.
- [85] R Secondo et al. “Reliable modeling of ultrathin alternative plasmonic materials using spectroscopic ellipsometry”. In: *Optical Materials Express* 9.2 (2019), pp. 760–770.
- [86] T. Koschny et al. “Resonant and antiresonant frequency dependence of the effective parameters of metamaterials”. In: *Phys. Rev. E* 68 (6 2003), p. 065602. DOI: 10.1103/PhysRevE.68.065602. URL: <https://link.aps.org/doi/10.1103/PhysRevE.68.065602>.
- [87] T. Koschny et al. “Reply to Comments on “Resonant and antiresonant frequency dependence of the effective parameters of metamaterials””. In: *Phys. Rev. E* 70 (4 2004), p. 048603. DOI: 10.1103/PhysRevE.70.048603. URL: <https://link.aps.org/doi/10.1103/PhysRevE.70.048603>.
- [88] Ricardo A. Depine and Akhlesh Lakhtakia. “Comment I on “Resonant and antiresonant frequency dependence of the effective parameters of metamaterials””. In: *Phys. Rev. E* 70 (4 2004), p. 048601. DOI: 10.1103/PhysRevE.70.048601. URL: <https://link.aps.org/doi/10.1103/PhysRevE.70.048601>.
- [89] AL Efros. “Comment II on “Resonant and antiresonant frequency dependence of the effective parameters of metamaterials””. In: *Physical Review E* 70.4 (2004), p. 048602.

APPENDICES

APPENDIX A - MATLAB CODES

A.1. Surface Plots of Permittivity vs. Wavelength and Fill Factor

```
1 %Surface plot for f from 0 to 1 – use 20 samples and contourf
2
3 clear;
4 clc;
5
6 %load permittivity data
7 load('Cu.mat');
8 load('TiO2.mat');
9 metal = Cu;
10 diel = TiO2;
11
12 e1 = horzcat(metal(:,1), (metal(:,2)+1i*metal(:,3)).^2); %from
    https://doi.org/10.1103/PhysRevB.6.4370\
13 e2 = horzcat(diel(:,1), (diel(:,2)+1i*diel(:,3)).^2); %from
    https://doi.org/10.1364/OE.20.015734
14
15 %interpolate data
16 wl = linspace(0.2,2,1000);
17
```

```
18 re1 = interp1(e1(:,1),real(e1(:,2)),w1,'pchip');
19 re2 = interp1(e2(:,1),real(e2(:,2)),w1,'pchip');
20 ie1 = interp1(e1(:,1),imag(e1(:,2)),w1,'pchip');
21 ie2 = interp1(e2(:,1),imag(e2(:,2)),w1,'pchip');
22
23 e11 = complex(re1,ie1);
24 e22 = complex(re2,ie2);
25
26 %use EMT to find new permittivities
27 c = 1;
28 for f = 0:0.05:1
29 e_TM = 1./(f./e11+(1-f)./e22);
30 e_TE = f.*e11+(1-f).*e22;
31
32 e_TM1 = real(e_TM);
33 e_TM2 = imag(e_TM);
34 e_TE1 = real(e_TE);
35 e_TE2 = imag(e_TE);
36
37 x(c,:) = e_TM1;
38 y(c,:) = e_TM;
39 c = c+1;
40
```



```
41 end
42
43 imagesc(wl,[0 1],real(log(x)));
44 c = colorbar;
45 c.Label.String = "Log of Real Part of Permittivity \epsilon'_{zz}
    }";
46 xlabel('Wavelength (\mum)')
47 ylabel('Fill Factor')
48
49 % figure;
50 % imagesc(wl,[0 1],imag(y));
51 % c = colorbar;
52 % c.Label.String = "Imaginary Part of Permittivity \epsilon''_{zz}
    }";
53 % xlabel('Wavelength (\mum)')
54 % ylabel('Fill Factor')
```

A.2. Surface Plots for Biaxial Metamaterials

```

1 clear ;
2 clc ;
3
4 %insert Ehsan's values
5 %Note: Ehsan measured zero loss in the TiO2
6 Ax = 1.562;
7 Bx = -0.009;
8 Cx = 0.00443;
9
10 Ay = 1.506;
11 By = -0.00219;
12 Cy = 0.00299;
13
14 Az = 1.591;
15 Bz = 0.01337;
16 Cz = 0.00082;
17
18 %We are using the Cauchy model:  $n(\lambda) = A + B/\lambda^2 + C/\lambda^4$ ;
19 wl = linspace (0.4 ,0.9 ,1000) ;
20 nx = Ax+Bx ./ wl.^2+Cx ./ wl.^4 ;
21 ny = Ay+By ./ wl.^2+Cy ./ wl.^4 ;

```

```
22 nz = Az+Bz./wl.^2+Cz./wl.^4;
23
24 load('Cu.mat');
25 metal = Cu;
26
27 e1 = horzcat(metal(:,1),(metal(:,2)+1i*metal(:,3)).^2); %from
    https://doi.org/10.1103/PhysRevB.6.4370\
28 re1 = interp1(e1(:,1),real(e1(:,2)),wl,'pchip');
29 ie1 = interp1(e1(:,1),imag(e1(:,2)),wl,'pchip');
30
31 e11 = complex(re1,ie1);
32 e22x = nx.^2;
33 e22y = ny.^2;
34 e22z = nz.^2;
35
36 c = 1;
37 for f = 0:0.05:1
38
39 exx = f.*e11+(1-f).*e22x;
40 eyy = f.*e11+(1-f).*e22y;
41 ezz = 1./(f./e11+(1-f)./e22z);
42
43 ezz1 = real(ezz);
```

```
44
45 x(c,:) = ezz1;
46 c = c+1;
47
48 end
49
50 imagesc(wl,[0 1],real(log(x)));
51 colorbar
52 xlabel('Wavelength (\mum)')
53 ylabel('Fill Factor')
```

A.3. Effective Medium Theory Calculations

```

1 clear ;
2 clc ;
3
4 %load permittivity data
5 load('Cu.mat');
6 load('TiO2.mat');
7 metal = Cu;
8 diel = TiO2;
9
10 e1 = horzcat(metal(:,1),(metal(:,2)+1i*metal(:,3)).^2); %from
    https://doi.org/10.1103/PhysRevB.6.4370\
11 e2 = horzcat(diel(:,1),(diel(:,2)+1i*diel(:,3)).^2); %from
    https://doi.org/10.1364/OE.20.015734
12
13 %interpolate data
14 w1 = linspace(0.38,0.9,1000);
15 % w1 = linspace(0.38,1.8,1000);
16
17 re1 = interp1(e1(:,1),real(e1(:,2)),w1,'pchip');
18 re2 = interp1(e2(:,1),real(e2(:,2)),w1,'pchip');
19 ie1 = interp1(e1(:,1),imag(e1(:,2)),w1,'pchip');
20 ie2 = interp1(e2(:,1),imag(e2(:,2)),w1,'pchip');

```

```
21
22 e11 = complex(re1 , ie1);
23 e22 = complex(re2 , ie2);
24
25 %use EMT to find new permittivities
26 f = 0.67;
27 e_TM = 1./( f ./ e11+(1-f) ./ e22); %Ezz
28 e_TE = f .* e11+(1-f) .* e22; %Exx , Eyy
29
30 n_TM = sqrt(e_TM);
31 n_TE = sqrt(e_TE);
32
33 e_TM1 = real(e_TM);
34 e_TM2 = imag(e_TM);
35 e_TE1 = real(e_TE);
36 e_TE2 = imag(e_TE);
37
38 % e_TE2 = -imag(hilbert(e_TE1));
39 % e_TM2 = -imag(hilbert(e_TM1));
40
41 %plot index of refraction
42 figure;
43 hold on;
```

```
44 yyaxis left;
45 plot(wl, real(n_TM))
46 plot(wl, real(n_TE))
47 ylabel('n')
48
49 yyaxis right;
50 plot(wl, imag(n_TM))
51 plot(wl, imag(n_TE))
52 hold off;
53
54 xlabel('Wavelength (nm)')
55 ylabel('k')
56 grid on
57 grid minor
58 title('Optical Constants of Hyperbolic Metamaterial')
59 legend('n_{x}', 'n_{y}', 'k_{x}', 'k_{y}')
60 xlim([.370 .900]);
61
62
63 %plot permittivities
64 figure('name', 'TM Mode');
65 hold on;
66 plot(wl, e_TM1)
```

```

67 plot(wl,e_TE1,'—')
68 y = ylim;
69 line([0.633 0.633],[y(1) y(2)],'color','r')
70 hold off;
71 % title("Real Part of \epsilon");
72 legend('\epsilon_{zz}','\epsilon_{xx}','\epsilon_{yy}');
73 xlabel('Wavelength (\mum)')
74 xlim([.370 .900]);
75 ylabel("\epsilon ")
76 grid on
77 grid minor
78
79 figure('name','Imaginary');
80 hold on;
81 plot(wl,e_TM2);
82 plot(wl,e_TE2,'—')
83 y = ylim;
84 line([0.633 0.633],[y(1) y(2)],'Color','r')
85 hold off;
86 legend('\epsilon_{zz}','\epsilon_{xx}','\epsilon_{yy}');
87 % title('Imaginary Part of \epsilon');
88 xlabel('Wavelength (\mum)')
89 xlim([.370 .900]);

```



```
90 ylabel('\epsilon')
```

```
91 grid on
```

```
92 grid minor
```

A.4. Effective Medium Theory Calculations for Biaxial Metamaterials

```

1 clear ;
2 clc ;
3
4 %insert Ehsan's values
5 %Note: Ehsan measured zero loss in the TiO2
6 Ax = 1.562;
7 Bx = -0.009;
8 Cx = 0.00443;
9
10 Ay = 1.506;
11 By = -0.00219;
12 Cy = 0.00299;
13
14 Az = 1.591;
15 Bz = 0.01337;
16 Cz = 0.00082;
17
18 %We are using the Cauchy model:  $n(\lambda) = A + B/\lambda^2 + C/\lambda^4$ ;
19 wl = linspace (0.4 ,0.9 ,1000) ;
20 nx = Ax+Bx ./ wl.^2+Cx ./ wl.^4 ;
21 ny = Ay+By ./ wl.^2+Cy ./ wl.^4 ;

```

```
22 nz = Az+Bz./wl.^2+Cz./wl.^4;
23
24 load('Cu.mat');
25 metal = Cu;
26
27 e1 = horzcat(metal(:,1),(metal(:,2)+1i*metal(:,3)).^2); %from
    https://doi.org/10.1103/PhysRevB.6.4370\
28 re1 = interp1(e1(:,1),real(e1(:,2)),wl,'pchip');
29 ie1 = interp1(e1(:,1),imag(e1(:,2)),wl,'pchip');
30
31 e11 = complex(re1,ie1);
32 e22x = hilbert(nx.^2);
33 e22y = hilbert(ny.^2);
34 e22z = hilbert(nz.^2);
35
36 f = 0.8;
37 exx = f.*e11+(1-f).*e22x;
38 eyy = f.*e11+(1-f).*e22y;
39 ezz = 1./(f./e11+(1-f)./e22z);
40
41 exx1 = real(exx);
42 exx2 = imag(exx);
43 eyy1 = real(eyy);
```

```
44 eyy2 = imag(eyy);
45 ezz1 = real(ezz);
46 ezz2 = imag(ezz);
47
48 %plot permittivities
49 figure('name','Real part of permittivity');
50 hold on;
51 plot(wl,exx1,'b')
52 plot(wl,eyy1,'k—')
53 plot(wl,ezz1,'r-.')
54 hold off;
55 title("Real Part of \epsilon");
56 legend('\epsilon_{xx}','\epsilon_{yy}','\epsilon_{zz}');
57 xlabel('Wavelength (\mu m)')
58 ylabel("\epsilon ")
59 grid on
60 grid minor
61
62 figure('name','Imaginary part of permittivity');
63 hold on;
64 plot(wl,exx2,'b')
65 plot(wl,eyy2,'k—')
66 plot(wl,ezz2,'r-.')
```

```
67 hold off;  
68 title('Imaginary Part of \epsilon');  
69 legend('\epsilon_{xx}', '\epsilon_{yy}', '\epsilon_{zz}');  
70 xlabel('Wavelength (\mu m)')  
71 ylabel('\epsilon''')  
72 grid on  
73 grid minor
```

A.5. Compare Effective Medium Theory Calculations to Measured Values

```

1 clear ;
2 clc ;
3
4 co = [230/255 97/255 1/255
5       253/255 184/255 99/255
6       %178/255 171/255 210/255
7       94/255 60/255 153/255]; %from Color Brewer 2.0
8 set(groot , 'defaultAxesColorOrder' ,co)
9
10 %load permittivity data
11 load('Cu.mat');
12 load('TiO2.mat');
13 metal = Cu;
14 diel = TiO2;
15
16 e1 = horzcat(metal(:,1) ,(metal(:,2)+1i*metal(:,3)).^2);
17 e2 = horzcat(diel(:,1) ,(diel(:,2)+1i*diel(:,3)).^2);
18
19 %interpolate data
20 w1 = linspace(0.38,0.9,1000);
21
22 re1 = interp1(e1(:,1) ,real(e1(:,2)) ,w1 , 'pchip');

```

```
23 re2 = interp1(e2(:,1),real(e2(:,2)),w1,'pchip');
24 ie1 = interp1(e1(:,1),imag(e1(:,2)),w1,'pchip');
25 ie2 = interp1(e2(:,1),imag(e2(:,2)),w1,'pchip');
26
27 e11 = complex(re1,ie1);
28 e22 = complex(re2,ie2);
29
30 %use EMT to find new permittivities
31 f = 0.69;
32 e_TM = 1./(f./e11+(1-f)./e22); %Ezz
33 e_TE = f.*e11+(1-f).*e22; %Exx,Eyy
34
35 n_TM = sqrt(e_TM);
36 n_TE = sqrt(e_TE);
37
38 e_TM1 = real(e_TM);
39 e_TM2 = imag(e_TM);
40 e_TE1 = real(e_TE);
41 e_TE2 = imag(e_TE);
42
43 %plot permittivities
44 figure('name','TM Mode');
45 hold on;
```

```

46 plot(wl,e_TM1)
47 plot(wl,e_TE1,'—')
48 % y = ylim;
49 % line([0.633 0.633],[y(1) y(2)],'color','r')
50 hold off;
51 legend('\epsilon_{zz}','\epsilon_{xx}','\epsilon_{yy}');
52 xlabel('Wavelength (\mum)')
53 xlim([.370 .900]);
54 ylabel("\epsilon ")
55
56 figure('name','Imaginary');
57 hold on;
58 plot(wl,e_TM2);
59 plot(wl,e_TE2,'—')
60 % y = ylim;
61 % line([0.633 0.633],[y(1) y(2)],'Color','r')
62 hold off;
63 legend('\epsilon_{zz}','\epsilon_{xx}','\epsilon_{yy}');
64 xlabel('Wavelength (\mum)')
65 xlim([.370 .900]);
66 ylabel('\epsilon ')
67
68 %Plot Measured Values Next to Obtained

```



```
69 load('HMM_91018_evenBetter.mat');
70 load('HMM_13119_21nm_better.mat');
71 load('HMM_30nm_mightBeBetter.mat');
72 dev1 = HMM_91018_evenBetter;
73 dev2 = HMM_13119_21nm_better;
74 dev3 = HMM_30nm_mightBeBetter;
75
76 %convert to permittivity
77 e11 = horzcat(dev1(:,1), (dev1(:,2)+1i*dev1(:,3)).^2);
78 e21 = horzcat(dev1(:,1), (dev1(:,4)+1i*dev1(:,5)).^2);
79 e12 = horzcat(dev2(:,1), (dev2(:,2)+1i*dev2(:,3)).^2);
80 e22 = horzcat(dev2(:,1), (dev2(:,4)+1i*dev2(:,5)).^2);
81 e13 = horzcat(dev3(:,1), (dev3(:,2)+1i*dev3(:,3)).^2);
82 e23 = horzcat(dev3(:,1), (dev3(:,4)+1i*dev3(:,5)).^2);
83
84 re11 = real(e11);
85 re21 = real(e21);
86 ie11 = imag(e11);
87 ie21 = imag(e21);
88 re12 = real(e12);
89 re22 = real(e22);
90 ie12 = imag(e12);
91 ie22 = imag(e22);
```

```

92 re13 = real(e13);
93 re23 = real(e23);
94 ie13 = imag(e13);
95 ie23 = imag(e23);
96
97 figure('name','TM Mode');
98 hold on;
99 plot(re21(:,1)/1000,re21(:,2),'-', 'LineWidth',4)
100 plot(re22(:,1)/1000,re22(:,2),'-.', 'LineWidth',4)
101 plot(re23(:,1)/1000,re23(:,2),':', 'LineWidth',4.8)
102 plot(wl,e_TM1,'—', 'LineWidth',4)
103 y = ylim;
104 line([0.64 0.64],[y(1) y(2)], 'color','r', 'LineWidth',4)
105 hold off;
106 xlabel('Wavelength (\mum)')
107 xlim([.370 .900]);
108 ylabel("\epsilon_{z}")
109 box on;
110 legend('15 nm', '20 nm', 'EMT', 'Location', 'northwest')
111 legend boxoff
112 set(findall(gcf,'-property','FontSize'),'FontSize',25)
113 set(findall(gcf,'-property','FontName'),'FontName','Times New
    Roman')

```

```

114 saveas(gcf,'re_z','epsc')
115
116 figure('name','TM Mode');
117 hold on;
118 plot(re21(:,1)/1000,ie21(:,2),'-','LineWidth',4);
119 plot(re22(:,1)/1000,ie22(:,2),'-.','LineWidth',4);
120 plot(re23(:,1)/1000,ie23(:,2),':', 'LineWidth',4.8);
121 plot(wl,e_TM2,'—','LineWidth',4)
122 hold off;
123 xlabel('Wavelength (\mum)')
124 xlim([.370 .900]);
125 ylabel('\epsilon_{z}''')
126 box on;
127 y = ylim;
128 line([0.64 0.64],[y(1) 150],'color','r','LineWidth',4)
129 set(findall(gcf,'-property','FontSize'),'FontSize',25)
130 set(findall(gcf,'-property','FontName'),'FontName','Times New
    Roman')
131 saveas(gcf,'im_z','epsc')
132
133 figure('name','TE Mode');
134 hold on;
135 plot(re11(:,1)/1000,re11(:,2),'-','LineWidth',4)

```

```

136 plot(re12(:,1)/1000,re12(:,2),'-.', 'LineWidth',4)
137 plot(re13(:,1)/1000,re13(:,2),':', 'LineWidth',4.8)
138 plot(wl,e_TE1,'—', 'LineWidth',4)
139 line([0.64 0.64],[-15 5], 'color','r', 'LineWidth',4)
140 hold off;
141 xlabel('Wavelength (\mum)')
142 xlim([.370 .900]);
143 ylabel("\epsilon_{x}")
144 box on;
145 set(findall(gcf,'-property','FontSize'),'FontSize',25)
146 set(findall(gcf,'-property','FontName'),'FontName','Times New
    Roman')
147 saveas(gcf,'re_x','eps')
148
149 figure('name','TE Mode');
150 hold on;
151 plot(re11(:,1)/1000,ie11(:,2),'-', 'LineWidth',4)
152 plot(re12(:,1)/1000,ie12(:,2),'-.', 'LineWidth',4)
153 plot(re13(:,1)/1000,ie13(:,2),':', 'LineWidth',4.8)
154 plot(wl,e_TE2,'—', 'LineWidth',4)
155 y = ylim;
156 line([0.64 0.64],[y(1) y(2)], 'color','r', 'LineWidth',4)
157 hold off;

```

```
158 xlabel('Wavelength (\mum)')
159 xlim([.370 .900]);
160 ylim([y(1) y(2)]);
161 xticks([0.4 0.6 0.8]);
162 ylabel('\epsilon_{x}')
163 box on;
164 set(findall(gcf,'-property','FontSize'),'FontSize',25)
165 set(findall(gcf,'-property','FontName'),'FontName','Times New
    Roman')
166 saveas(gcf,'im_x','epsc')
```

A.6. Plotting the Hyperbolic Isofrequency Curve

```

1 % Next: Add the sphere for the Si interface
2 % I can also convert to polar coordinates
3
4 clear;
5 clc;
6 %From EMT:
7 wl = 633;
8 k0 = 2*3.14/wl;
9 ezz = 22.33;
10 exx = -5.934;
11
12 %Solve Dispersion Relation for kz:
13 %  $k_0^2 = (k_x.^2+k_y.^2)/ezz+k_z.^2/exx$ ;
14 %  $k_0^2 - k_z.^2/exx = (k_x.^2+k_y.^2)/ezz$ ;
15 %  $k_z.^2/exx = -(k_x.^2+k_y.^2)/ezz + k_0^2$ 
16 %  $k_z = \sqrt{-exx .* (k_x.^2+k_y.^2) ./ ezz + k_0^2}$ ;
17
18 syms kz(kx,ky)
19 kz(kx,ky) = sqrt(-exx * (kx^2+ky^2)/ezz + k0^2);
20 fsurf(kz, [-.1 .1 -.1 .1], 'MeshDensity',40, 'LineStyle', 'none')
21 % axis off
22 hold on

```

```
23 fsurf(-kz, [-.1 .1 -.1 .1], 'MeshDensity',40, 'LineStyle', 'none')
24 hold off
25
26 camlight(110,70)
27 brighten(0.6)
28 xlabel('k_{x}')
29 ylabel('k_{y}')
30 zlabel('k_{z}')
31 set(gca, 'xtick', [])
32 set(gca, 'ytick', [])
33 set(gca, 'ztick', [])
```